Photochemical Escape of Oxygen from Mars: first results from MAVEN in situ data

Robert J. Lillis[1], Justin Deighan[2], Jane Fox[3], Stephen W. Bougher[4], Yuni Lee[4], Michael R. Combi[4], Thomas E. Cravens[5], Ali Rahmati[1], Paul Mahaffy[6], Mehdi Benna[6], Meredith K. Elrod[6], James P. McFadden[1], Robert. E. Ergun[2], Laila Andersson[2], Christopher M. Fowler[2], Bruce M. Jakosky[2], Ed Thiemann[2], Frank Eparvier[2], Jasper Halekas[7], François Leblanc[8], Jean-Yves Chaufray[8]

[1]Space Sciences Laboratory, University of California Berkeley, 7 Gauss Way, Berkeley, CA 94720, USA

[2] Laboratory for Atmospheric and Space Physics, 3665 Discovery Drive, University of Colorado, Boulder, CO 80309, USA

[3]Department of Physics, Wright State University, Dayton, Ohio, United States

[4]Department of Climate and Space Sciences and Engineering, University of Michigan, Ann Arbor, Michigan, USA

[5]Department of Physics and Astronomy, University of Kansas, Lawrence, Kansas, USA.

[6]NASA Goddard Space Flight Ctr., Greenbelt, MD, USA

[7]Department of Physics and Astronomy, University of Iowa, Iowa city, Iowa, USA

[8]LATMOS/CNRS, Université Pierre et Marie Curie, Paris, France

Key points:

1. Photochemical O escape fluxes from dissociative recombination of O_2^+ are calculated from MAVEN in situ data.
2. Escape rates of 1.2 - 5.5 x 10^{25} s^{-1} are consistent with previous models and those derived from other MAVEN observations.
3. We find a power law exponent of 2.6 for the EUV dependence of escape rate, implying several hundred millibars of oxygen loss over 3.5 billion years.

Corresponding author: Robert Lillis, rlillis@SSL.Berkeley.edu, 510-642-6211

Abstract

Photochemical escape of atomic oxygen is thought to be one of the dominant channels for Martian atmospheric loss today and played a potentially major role in climate evolution. MAVEN is the first mission capable of measuring, in situ, the relevant quantities necessary to calculate photochemical escape fluxes. We utilize 18 months of data from three MAVEN instruments: LPW, NGIMS and STATIC. From these data we calculate altitude profiles of the production rate of hot oxygen atoms from the dissociative recombination (DR) of O_2^+ and the probability that such atoms will escape the Mars atmosphere. From this we determine escape fluxes for 815 periapsis passes. Derived average dayside hot O escape rates range from 1.2 to 5.5 x 10^{25} s^{-1} depending on season and EUV flux, consistent with several pre-MAVEN predictions and in broad agreement with estimates made with other MAVEN measurements. Hot O escape fluxes do not vary significantly with dayside solar zenith angle or crustal magnetic field strength, but depend on CO_2 photoionization frequency with a power law whose exponent is 2.6 ± 0.6, an unexpectedly high value which may be partially due to seasonal and geographic

sampling. From this dependence and historical EUV measurements over 70 years, we estimate a modern-era average escape rate of 4.3 x 10^{25} s^{-1}. Extrapolating this dependence to early solar system EUV conditions gives total losses of 13, 49, 189, and 483 mb of oxygen over 1, 2, 3, and 3.5 Gyr respectively, with uncertainties significantly increasing with time in the past.

Keywords:

Mars, atmosphere, oxygen, photochemical, escape.

1 Introduction

Photochemical escape in planetary atmospheres is a process by which a) an exothermic chemical reaction produces an upward-traveling neutral particle whose velocity exceeds the planetary escape velocity and b) the particle is not prevented from escaping through any subsequent collisions with thermal neutrals. At Mars, photochemical escape is thought to be the dominant loss process for neutrals heavier than hydrogen today [*Lammer et al.*, 2008], likely several times larger than heavy ion escape, and thus one of the major pathways for atmospheric escape over the history of Mars. The photochemical escape of O, N and C atoms is the result of photodissociation, photodissociative ionization and electron-impact dissociative ionization of the primary neutral constituents primary CO_2, CO, N_2, O and O_2, as well as dissociative recombination (DR) of the ion species N_2^+, CO^+, NO^+ and O_2^+ [*Fox and Hać*, 2009]. By approximately 2 orders of magnitude the dominant escaping atom is O (cf. table 3 of *Brain et al.* [2015]), mostly the result of DR of O_2^+, the process upon which we will focus in this study.

The critical altitude region for photochemical escape is within a few scale heights of the exobase (i.e. 170-250 km), i.e. the region sufficiently low in altitude that substantial amounts of O_2^+ are created, but where the mean free path is sufficiently large that energized hot O atoms can escape the atmosphere in substantial numbers without first losing too much energy through collisions.

Several numerical models of photochemical escape of O from Mars have been developed in recent years using input from the two vertical profiles recorded by the Viking Landers [*Hanson et al.*, 1976; *Nier et al.*, 1976] and global circulation models [*Bougher et al.*, 1999; 2000; *Gonzalez-Galindo et al.*, 2013]. Photochemical escape rates range from 1.0 to 6.0 x 10^{25} s^{-1} for equinox solar minimum conditions and from 4.0 to 22.0 x 10^{25} s^{-1} for equinox solar maximum conditions, with an average of 2.75 for the ratio between the former and latter conditions [*Chaufray et al.*, 2007; *Cipriani et al.*, 2007; *Fox and Hac*, 2014; *Fox and Hać*, 2009; *Groller et al.*, 2014; *Hodges*, 2002; *Krestyanikova and Shematovich*, 2005; *Lee et al.*, 2015b; *Valeille et al.*, 2009a; *Valeille et al.*, 2009b].

In addition, remote observations of Mars' oxygen exosphere from MAVEN have provided photochemical escape rate estimates. *Rahmati et al.* [2016] showed that pickup oxygen ion distributions measured by the Solar Wind Ion Analyzer [*Halekas et al.*, 2015] from solar moderate (December 2014) and solar minimum (December 2015) conditions are consistent with an oxygen exosphere structure which implies a modeled escape rate of 7 x 10^{25} s^{-1}. Also, *Lee et al.* [2015a] modeled the altitude profiles of 130.4 nm oxygen emission from the Martian exosphere for solar moderate, perihelion conditions (where the escape rate was ~3.5 x 10^{25} s^{-1}), finding that the intensity was a factor of ~1.5-2 lower than that measured by the Imaging Ultraviolet Spectrometer [*Deighan et al.*, 2015; *McClintock et al.*, 2015] for the same period. Since this emission is optically thin, this is consistent with a modeled escape rate of ~5.2 -

7 x 10^{25} s^{-1} from O_2^+ dissociative recombination. Lastly *Cravens et al.* [2016] conducted a simplified theoretical analysis of photochemical escape from DR of O_2^+ in the Mars atmosphere, concluding that under simplified assumptions such as an isothermal CO_2-only atmosphere, photochemical escape rates should be proportional to solar EUV irradiance and inversely proportional to the collision cross-section between hot O and CO_2.

In this paper we present the first estimates of photochemical escape fluxes of atomic oxygen calculated from in situ data collected in the Martian thermosphere and ionosphere by the MAVEN spacecraft [*Jakosky et al.*, 2014]. Section 2 discusses the data used and the caveats therewith. Section 3 describes the method of calculating photochemical escape and provides an example. Section 4 describes the results, comparing derived photochemical escape fluxes with season, solar zenith angle and EUV photoionization frequencies, as well as establishing a range of likely escape fluxes for the modern era going back to 1947 and finally extrapolation backward in time to escape rates and total oxygen loss over the last several billion years. Section 5 discusses comparisons with earlier modeling efforts, uncertainties, complementary MAVEN remote-sensing measurements and the trade-off between the kind of hot neutral escape described in this paper versus the direct energization of molecular ions via electric fields. Section 6 discusses conclusions and future work.

2 Data used in this study

Although photochemical escape of O cannot be directly measured by MAVEN (no instrument currently exists to measure the velocities of hot neutral atoms in the appropriate energy range of < 10 eV), all of the important quantities upon which it depends are measured in situ in the Mars upper atmosphere,

typically on at least every other orbit. We use in situ data from three instruments collected below 400 km during 1662 orbits spanning February 10, 2015 to July 31 2016. We obtain temperatures and densities of ambient electrons measured by the Langmuir Probe and Waves (LPW) experiment [*Andersson et al.*, 2015; *Andrews et al.*, 2015; *Ergun et al.*, 2015; *Fowler et al.*, 2015]. We also use temperatures of thermal O_2^+ ions measured by the SupraThermal And Thermal Ion Composition (STATIC) experiment [*McFadden et al.*, 2015]. Finally, we use densities of thermal O_2^+ ions and the thermal neutral species CO_2, CO, N_2 and O measured by the Neutral Gas and Ion Mass Spectrometer (NGIMS)[*Mahaffy et al.*, 2014]. Other measured neutral species make up less than 1% of the density at the relevant altitudes [*Mahaffy et al.*, 2015].

Here we describe a number of data selection and preparation issues. First, we choose to use only data from the inbound portion of each periapsis pass because reactive neutral species build up in the NGIMS instrument during periapsis, meaning that the background count rate is substantially lower for inbound compared to outbound passes. Second, due to imperfectly subtracted backgrounds above ~280 km, we replace all atomic oxygen densities data above 280 km with an exponential function and a single scale height equal to the average scale height measured between 220 km and 280 km. It is important to note that this extrapolation has a negligible effect on derived escape fluxes because more than 90% of the escape flux originates below 280 km. Third, both NGIMS and STATIC measure thermal ion densities, but we choose to use NGIMS as the sole source of O_2^+ densities in this study due to an ongoing and as-yet-unresolved issue of low energy ion suppression in STATIC. Note that, due to its very narrow field of view, NGIMS is optimized for measuring the kind of isotropic particle distributions we see in the photochemically dominated ionosphere; at higher altitudes above ~300 km ions can be quite directional

and therefore NGIMS underestimates ion densities. However, the vast majority of escaping ions are produced below 250 km, so this underestimation should not significantly affect the results. Fourth, we only use passes where a reliable electron temperature is derived by LPW at all altitudes. Fifth, we note that NGIMS cannot measure both ions and reactive neutral species (i.e. CO and O) on the same periapsis pass due to the need to warm up the filament that is used to ionize neutrals coming into the open source aperture [*Mahaffy et al.*, 2014]. For this reason, we use different subsets of the 1662 orbits to calculate dissociative recombination rates and escape probabilities, according to the availability of the relevant data in each set of orbits, as described in the next section. We will also compare derived escape fluxes with relevant parameters such as Mars season, crustal magnetic field strength, solar zenith angle and CO_2 photo ionization rate (see Appendix A).

3 Method for calculating photochemical escape of oxygen

In order to determine photochemical escape fluxes of hot oxygen from in situ measurements, we must separately calculate two different quantities as a function of altitude *z*: 1) the production rate of hot oxygen atoms from O_2^+ DR and 2) the probability that, once produced, a hot O atom will escape the atmosphere. The hot O production rate R, in number per cubic centimeter per second, is given by twice the DR rate (each reaction produces 2 oppositely-directed O atoms):

$$R_{hot\ O}(z) = 2n_e(z)n_{O_2^+}(z)k\big(T_e(z)\big) \quad (1)$$

where $n_{O_2^+}(z)$ and $n_e(z)$ are the densities of the ambient thermal O_2^+ ions and electron respectively and *k* is the DR rate coefficient. The DR cross section depends primarily on electron velocity, and thus the

rate coefficient *k* depends on electron temperature, with a dependence best fit by the following expression [e.g. *Petrignani et al.*, 2005]:

$$k = 1.95 \times 10^{-7} \left(\frac{300}{T_e}\right)^{0.70} cm^3 s^{-1} \quad (2)$$

The probability of escape for an O atom produced by DR depends on two main factors: the initial energy of the atom and the column density and composition of the gas above the altitude where it was 'born'. DR occurs via four main channels with the resulting O atoms each leaving with half of the exothermic energy in the center of mass frame of the electron-ion collision. The four channels are given in Table 1 with their relative likelihoods [*Fox and Hać*, 2009]:

Place Table 1 here

The upper two of these reactions result in individual O energies in excess of the escape energy (at 200 km altitude) of 1.98 eV. The final energies of the resulting O atoms in the atmospheric rest frame depend on the relative velocities of the electrons and O_2^+ ions and hence on electron and ion temperature. We note that this dependence on ionospheric plasma temperatures is small, since such temperatures are typically <0.1 eV [*Ergun et al.*, 2015] at the altitudes (~180-250 km) from which most photochemical escape occurs, but we include them for completeness. Therefore, the energy distribution of nascent hot oxygen atoms (and the fraction of those with energies above the escape energy) varies with altitude, from close to 4 delta functions (with the energies shown above) at lower thermospheric altitudes to a somewhat broader distribution in the exosphere. An example of the altitude-energy distribution of hot O atoms is shown in Figure 1.

For each set of neutral density and electron and ion temperature profiles, we run a three-dimensional Monte Carlo hot atom transport model to calculate escape probabilities as a function of altitude. We assume the atmosphere is spherically symmetric with the same altitude profile everywhere. Hot O atoms start at a set altitude and are given random directions and an initial energy drawn at random from the initial energy distribution for that altitude (mentioned in the previous paragraph). They are propagated through collisions with thermal neutrals, using the cross-sections shown in Table 2. Angular-dependent cross-sections are assumed to be the same for all species and are taken from *Kharchenko et al.* [2000]. We run this model at each altitude until 2500 hot oxygen atoms escape (i.e. reach the top of the simulation with escape energy or greater). 2500 divided by the number of atoms spawned gives the escape probability. Starting from 400 km we work down in altitude until the escape probability falls below 5×10^{-5}.

Once we have calculated altitude profiles of the hot O production rate and the hot O escape probability, we simply multiply these two quantities together at each altitude step to get the production rate of escaping hot O. We then integrate with respect to altitude to get the hot O escape flux for that particular periapsis pass. **Figure 2** is a flowchart of this calculation, relating the quantities measured by MAVEN, formulae derived from experiment, models and calculated values.

Place Table 2 here

As mentioned in section 2, the profiles of all necessary quantities shown in the left magenta boxes in **Figure 2** are not measured in the same orbit. Therefore, for each of the 485 orbits where we are able to determine the hot oxygen production rate profile (i.e. where full profiles of electron temperature,

electron density and O2+ density are measured; see the lower blue box in **Figure 2**), we multiply by an escape probability profile (upper blue box in **Figure 2**) that is the mean of the escape probability profiles determined (from the neutral density, ion temperature and electron temperature) measured on the previous and subsequent orbits. An example calculation is shown in **Figure 3** for a periapsis in April 2015, during MAVEN's second "deep dip" campaign in the vicinity of the subsolar point, when the periapsis altitude was ~130 km. The derived escape flux of ~1.4 x 10^7 O atoms per square centimeter per second is fairly typical of the dayside during the data collection period, as discussed in the next section.

Note that this calculation assumes that the measured profiles are precisely vertical, when in fact the spacecraft travels ~2000 km laterally during each inbound pass below 500 km. However, the vast majority (>90%) of the total escape originates between ~180 and 280 km, during which time the spacecraft moves ~750 km. Indeed, *Lillis et al.* [2015] reported <10% differences in hot O escape fluxes calculated using radial versus along-track profiles through the Mars Thermospheric Global Circulation Model[*Bougher et al.*, 1999; 2000].

We also calculated uncertainty for each derived value of escape flux. This is done by propagating the published uncertainties in the electron density, O2+ density and electron temperature through to calculate the altitude profile of uncertainties in the production rate of hot O. This is then convolved with the uncertainty in the escape probability profile, which is simply taken to be half the difference between the probability profiles calculated using the neutral densities measured on the previous and subsequent orbits. The result is the uncertainty in the altitude profile of the production of escaping hot O. We then

propagate this uncertainty through each step of the integration with respect to altitude to arrive at an uncertainty in each escape flux measurement. These are typically several tens of percent and are shown in Figure 7a.

Place Figures 1 and 2 here

4 Results

4.1 Data coverage

Figure 4 shows coverage for all data used in this study. Panel a) shows how the total CO_2 photoionization rate at Mars (see appendix A) decreases by up to 45% with time as Mars moves further from the sun toward and past aphelion. The short-term variations are due to solar rotation as active regions on the sun's surface rotate in and out of view of Mars. Panels b) and c) show the spacecraft location below 250 km in Mars-solar-orbital (MSO) coordinates and planetary coordinates respectively. The data set begins at the dusk terminator, that continues across the subsolar point and continues out to about 60° solar zenith angle on the dawn side during a period of relatively high solar EUV irradiance. There are a substantial number of profiles in this timeframe (particularly between 20° and 45°) which suffered from unreliable electron temperature profiles due to large negative spacecraft potentials and so are unusable. There is also a data gap coinciding with solar conjunction and other technical problems with NGIMS for all of June 2015. July and August 2015 are on the nightside in the southern hemisphere. Periapsis then crosses the dayside from southern hemisphere dusk in September 2015 to northern hemisphere dawn in January 2016 for aphelion atmospheric and EUV conditions. It then continues into the northern hemisphere night side, before crossing back into daylight from the North Pole in February

2016 and crossing the dawn terminator once more in May 2016 and continuing towards the anti-solar point in northern spring. The geographic coverage is broad in longitude as expected as the planet rotates underneath MAVEN's orbit.

Place Figure 3 here

4.2 Escape fluxes

4.2.1 Broad trends

All 815 derived values of the escape flux of O atoms from DR of O_2^+ are shown in Figure 5 and Figure 6. **Figure 5** shows escape fluxes are substantially higher in early 2015, when Mars is comparatively close to the sun and the sun is reasonably active (approximately solar moderate), ranging 4 to 8 x 10^7 /cm^2/s. As Mars recedes and solar activity diminishes, photoionization frequency drops and average escape fluxes drop correspondingly during the same period. By the time MAVEN's periapsis is on the dayside again in October 2015, ionization frequencies have dropped by ~40% from their highest values and derived escape fluxes have dropped by a factor of two or more. From then until mid-2016, both ionization frequencies and dayside escape fluxes stay generally low.

In addition, there are some interesting features beyond this general trend positive dependence on EUV flux. The first is that photochemical escape is reasonably constant with respect to solar zenith angle over the parts of the dayside MAVEN sampled and where full profiles were available. This is seen clearly in **Figure 5** but particularly in Figure 6a, b. However, beyond ~100° solar zenith angle, we see a very wide range in escape fluxes, varying by more than three orders of magnitude. This is somewhat to be

expected, given the highly variable and inhomogeneous nature of the Mars nightside ionosphere, which is due to strong temporal and geographic variability in electron precipitation and hence ionization [e.g. *Lillis et al.*, 2011; *Němec et al.*, 2011].

The second pattern is that we see an apparent dawn-dusk asymmetry in escape fluxes. **Figure 5**b and particularly Figure 6b show that escape fluxes are typically higher on the dusk side than the dawn side, with the difference increasing with solar zenith angle. However, dawn and dusk, both sampled twice during the dates in question, were sampled at different seasons and latitudes. Therefore, while such an asymmetry is physically plausible (ions can survive for some time after sunset but have not yet been produced before sunrise and cross-terminator flow seems to favor dusk side [*Benna et al.*, 2015]), confirmation of a dawn-dusk asymmetry in photochemical escape awaits more sampling.

Place Figure 4 here

Figure 6c shows that, within this limited data set, there is no statistically significant correlation between crustal magnetic field strength and derived photochemical escape fluxes, either on the day or night side. Note however that this comparison would only reveal the broadest trends, since the fluxes are classified according to the magnitude of the crustal magnetic field at 400 km at the latitude and longitude of the periapsis. A more detailed study (left to future work) would examine the specific magnetic topology and magnitude at each individual point where the production rate of escaping hot O is calculated.

4.2.2 Short-term variability

Factors of ~2-3 variability within a short time span are not unusual. This 'statistical' variability arises both natural variability in the physical system and our sampling of that system. Let's first discuss natural

variability. First, although variations in total neutral mass density should not affect escape fluxes (because the ionospheric profile should simply move up and down in response), relative changes in the densities of different neutral species will affect escape fluxes in two different ways: a) CO_2 is the main source for the O_2^+ ions that dissociatively recombine [*Schunk and Nagy*, 2000] and b) different species have different cross-sections for collisions with hot O atoms that are produced from the recombination. Such relative density changes between species are caused by tides and gravity waves in the Martian thermosphere and are not just expected [e.g. *Medvedev and Yigit*, 2012], but have been observed in data from both the Imaging Ultraviolet Spectrometer (IUVS) and NGIMS [*England et al.*, 2016]. Second, the dayside ionosphere can be quite 'lumpy' due to ion transport near and above the exobase along crustal magnetic field lines, as was observed in radar echoes from the MARSIS instrument on Mars Express [*Morgan et al.*, 2008]. Third, despite being a minor contributor to total ionization on the dayside, impact ionization from precipitating electrons and ions tends to peak at higher altitudes (160-200 km) [*Lillis et al.*, 2011; *Lillis et al.*, 2008] than photoionization (~130 km) [e.g. *Hanson et al.*, 1977] and thus can play a proportionally larger role in determining O_2^+ densities at the altitudes from which escape is occurring. This precipitation is temporarily highly variable and therefore can also contribute to variability. Fourth, currents in the dayside ionosphere, driven by neutral winds, electric fields and magnetic gradient/curvature drifts can drive local variability in both electron and ion densities [*Fillingim et al.*, 2012; *Riousset et al.*, 2013].

Place Figure 5 here

In addition, part of the statistical variability we see is due to uncertainty in our input profiles. Uncertainties in electron and ion densities are typically several tens of percent [*Benna et al.*, 2015; *Ergun et al.*, 2015]. Also, more importantly, the escape probability profile varies exponentially with altitude and is calculated assuming the average of the neutral densities measured on the previous and subsequent orbits; factors of 2-3 orbit-to-orbit variability are not unusual in the Mars thermosphere [e.g. *Keating et al.*, 1998] and so could also plausibly account for this variability.

4.2.3 Correlation with solar EUV irradiance

Next we examine the variability in escape fluxes due to changing EUV irradiance. We choose to use photoionization frequency instead of irradiance, because it more directly determines the rate of production of molecular oxygen ions (see Appendix A for details), which lead to photochemical escape when they dissociatively recombine. This relationship between ionization frequency and photochemical escape is especially important because the early sun was substantially brighter in the EUV [*Ribas et al.*, 2005] (see section 4.5). Figure 7a shows all 594 of the derived values of O escape flux taken with solar zenith angles less than 95° (i.e. dayside) as a function of the photoionization frequency, along with binned averages and standard errors (standard deviations divided by the square of the number of samples). We fit this distribution with the function:

$$F_{escape} = BI^{\gamma} \quad (3)$$

where F_{escape} is the derived escape flux in #/cm^2/s, I is the measured ionization frequency in s^{-1} and B, γ are fitting parameters. We did not add a constant term to the right-hand side of the equation 3 because solar EUV is by far the dominant source of ionization the Martian atmosphere and because test fits

resulted in a consistently negative constant term, which is unphysical in the context of photochemical escape.

Reduced chi-square values were calculated using the average and standard error for every bin (black symbols in Figure 7). All fits within the 1-sigma and 3-sigma error ellipsoids are shown in dark and light gray respectively and a histogram of power law indices for those fits are shown in Figure 7b. The full two-dimensional chi-square space is shown in Figure 7c. The best fit exponent is 2.64, but with a moderate spread within 1-sigma. This is unexpectedly high, as we discuss below.

4.2.4 An unexpected relationship to solar EUV irradiance

In general, EUV irradiance should be the main variable factor for the three primary quantities for determining photochemical escape : a) photoionization rates, which determine electron and ion densities, b) electron temperatures which determine recombination rates (these two directly determine the production rate of hot O atoms, see equation 1) and c) thermospheric/exospheric neutral temperatures which affect hot O transport [e.g. *Zhao and Tian*, 2015]. In a theoretical examination of photochemical escape of O, *Cravens et al.* [2016] show that, under a set of simplifying assumptions including an isothermal CO_2 atmosphere and a single EUV wavelength, photochemical escape flux should depend linearly on solar EUV irradiance only and no other variable factor. However, as the dashed red line in Figure 7a shows, the best-fit linear function does not fit the derived escape fluxes very well. What explanations may there be for the much-higher best-fit power law exponent of ~2.6?

Here it is appropriate to distinguish between non-EUV factors potentially affecting escape fluxes that are expected to vary with Mars season, and factors that are expected to vary with solar activity alongside

EUV irradiance. The effects of these should ideally be quantified and separated and their effects removed from the comparison with solar EUV flux. The former could then be removed from any long-term extrapolation to past, higher EUV levels, while the latter could be included as a separate dependence on heliospheric conditions such as solar wind velocity, density and magnetic field. Such a separation and quantification is beyond the scope of this paper. Nonetheless, it is useful to discuss these non-EUV factors.

Let us first address the seasonally varying factors, wherein it is important to reiterate that we are not deriving global photochemical escape rates in this study, but local escape fluxes in discrete swaths of the atmosphere. Our periapsis measurements are taken along a single 'track' in latitude, solar zenith angle and Mars season as MAVEN's orbit precesses in time (see **Figure 4**). Therefore, any conclusions we may draw about the dependence of escape flux on EUV irradiance are subject to the assumption that all the sources of short-term variability discussed in the previous subsection "wash out" over seasonal timescales and across latitudes and solar zenith angles: gravity waves and tides, ion transport, charged particle impact ionization and ionospheric currents. However, of these, Martian gravity waves are known to be stronger in the southern hemisphere in southern spring and summer near perihelion [*Wright*, 2012] and rates of charged particle precipitation are known to be higher when solar wind pressure is higher [*Lillis and Brain*, 2013], as it is when Mars is closer to the sun near perihelion. As mentioned, we shall not attempt to quantitatively assess what these impacts may be, but they may serve to enhance the positive correlation between hot O escape fluxes and photoionization frequency we see in Figure 7, since all of the high EUV measurements (ionization frequency > 4.5 x 10^{-7} s^{-1}) were taken in southern summer and early autumn.

Next we address those factors which are expected to vary with solar activity alongside EUV. Ion transport, ionospheric currents, charged particle precipitation (both ionization and heating of neutrals) may all reasonably be expected to increase near the exobase with increased heliospheric activity. The former two may have a positive or negative effect on ion densities in different geographic regions or overall, while impact ionization from charged particles should increase hot O production. In other words, it is difficult to assess to what degree these factors, all of which should roughly correlate with solar EUV, may be contributing to a higher best-fit power law in Figure 7. Even if we could separate these effects from those of EUV, a further complication is that, unlike solar EUV irradiance [*Ribas et al.*, 2005], the historical record of solar wind speed and density and frequency and intensity of heliospheric disturbances is quite uncertain, due primarily to uncertainty in early solar rotation rates [e.g. *Johnstone et al.*, 2015]. Nonetheless, in this study we will use the range of functional forms of EUV dependence shown in Figure 7 in our extrapolations to both modern-day (section 4.4) and ancient (section 4.5) conditions.

Place Figure 6 here

4.3 Understanding variability in escape fluxes

Let us now turn attention to the root causes of higher or lower derived photochemical escape fluxes in terms of the atmospheric and ionospheric conditions that determine those fluxes. As explained in Section 3, the photochemical escape flux at a given altitude depends not only on the plasma density there, but on the total column of neutral density above that altitude and its composition, as well as on electron temperature (which determines the recombination rate coefficient). In order to gain a clearer

picture of the origin of the variability we see in **Figure 5**, Figure 6 and Figure 7, let us examine the profiles of these important determining factors of escape flux for three representative time intervals. These intervals were chosen for their combination of season, solar zenith angle and EUV irradiance to illustrate how the profiles of different quantities determine the escape flux. They are shown in Table 3 and **Figure 5**a. Interval 1 (black) is near the dusk terminator just after perihelion during the highest period of EUV irradiance observed by MAVEN (though not historically high, see Figure 10) so far. Interval 2 (pink) is near noon at mid-southern latitudes at the very lowest EUV flux observed just before aphelion and interval 3 (gray) is near the dawn terminator near the equator for a somewhat higher EUV irradiance typical of most of 2016. Recall that the ion and electron temperatures do not have a significant impact on the energy distribution of the newly-created hot O atoms, but the electron temperature is important in that it determines the rate of their creation.

First we note that the markedly higher electron and ion densities (**Figure 8**a, b) seen for interval 1 (black) are most of the reason why the production rate of hot O is much higher than for the other intervals, though the slightly lower recombination rate (**Figure 8**d) due to lower electron temperature (**Figure 8**c) plays a minor role too. However we also note that the bulk of the escaping hot O atoms originate from a higher altitude because the lower atmosphere is warmest near perihelion and therefore the exobase mass density is higher (**Figure 8**e), pushing both the ionosphere and the escape region 25 km higher than interval 3 and ~15 km higher than interval 2 (**Figure 8**f).

Also, we notice that the peak and total production rate of escaping atoms is higher during interval 3 (pink) than Interval 2 (gray). This is due to higher EUV irradiance causing higher peak plasma densities.

We also notice that the escaping atoms originate from a lower altitude because the lower Mars atmosphere is cooler (i.e. lower densities at the homopause) near dawn at 40° North latitude in northern spring for interval 2 than at noon at ~35° south latitude in southern winter for interval 3.

Figure 9 is an attempt to show intuitively that the reason for the different photochemical escape fluxes during these intervals lies in the different paths they take through the parameter space defined by the production of hot O (mostly determined by plasma density) and the retardation of its escape by collisions with thermal neutrals (mostly O and CO_2). Panel a) shows binned averages of the production rate of escaping hot O atoms as a function of column mass density (on an inverted scale so that its logarithm is a proxy for altitude) and O_2^+ density. The contours show that there is a 'sweet spot' in altitude for the production of escaping hot O, where the plasma density is high enough to cause a large O production rate, but the column density above is sufficiently low that the O can escape. Also shown are the paths taken by the average values of these quantities for the three intervals. It is important to note that the total escape flux is the integral of the production rate of escaping O, with respect to altitude, along this path. Thus it is clear (as it is from **Figure 8**f) that interval 1 has a higher escape flux than interval 2 because its average altitude profile traverses a higher plasma density with respect to the same range of column mass densities. **Figure 9**b shows the binned production rate of escaping O atoms with respect to O_2^+ density and electron temperature, limited to a narrow range of column mass densities (**1 to 3 x 10^{-8} g/cm^2**) showing the comparatively modest, but non-negligible, effect of electron temperature on escape fluxes.

Place Figure 8 here

Place Table 3 here

4.4 Estimates of global escape rates in the present-day epoch

Given that there is no discernible trend in escape fluxes with solar zenith angle on the dayside (see Figure 6), it is reasonable to simply multiply our escape fluxes by the area of the dayside of Mars up to 103° SZA: 2.45 $\pi (R_{Mars} + 200\ km)^2$ = 9.92 x 10^{17} cm^2, where R_{Mars} is the area-weighted average radius of the martian areoid (3389.9 km). Given the range of altitudes over which the production of escaping O occurs, it is reasonable to use a convenient area of 10^{18} cm^2, by which we can multiply all escape flux numbers in order to get global escape rates.

One of the prime goals of the MAVEN mission is to constrain the total loss of atmosphere over Martian history. In order to build a baseline from which we may extrapolate photochemical O escape rates backward in time, we must estimate the average escape rate over the modern epoch, i.e. over the range of solar EUV irradiance conditions that exist in the modern era. The results are shown in Figure 10, where panel a) shows the weekly photoionization frequency (calculated as described in Appendix A) since 1947 on the basis of direct measurements back to 2002, satellite measurements of solar Lyman alpha irradiance back to 1978 and ground-based measurements of F10.7 solar radio flux prior to 1978 [*Thiemann et al.*, 2016]. Panel b) shows the range of escape rates over the same time that are consistent with the power law indices within the 1-sigma χ^2 error ellipsoid of fits to the EUV dependence of derived escape rates shown in Figure 7. Panel c) shows a histogram of every escape rate data point shown in panel b). Although there are a few points (for larger power law indices, perihelion and solar maximum) over the decades where rates can reach 4 x 10^{26} s^{-1}, 80% of values lie within the range of 1.1 to 9.1 x 10^{25} s^{-1}. With values that vary over such a large range, it is reasonable to characterize the standard

deviations in terms of logarithms, giving us a mean (lower bound, upper bound) of 4.3 (1.9, 9.6) x 10^{25} O atoms per second in the modern epoch.

Place Figure 9 here

4.5 Estimates of historical atmospheric escape rates and loss

We now have in hand a modern-day estimate for photochemical escape rates and a range of dependences on EUV flux. This allows us to make estimates of escape rates at earlier times in solar system history. We are specifically concerned with the evolution of solar ultraviolet irradiance from ~10 to 89 nm, i.e. photons capable of ionizing CO_2 (see Figure 13c). Several studies have been carried out using observations of G-type (i.e. sun-like) stars, each fitting the observed decrease in irradiance with the functional form $t^{-\beta}$, where t is the stellar age in billions of years. *Ayres* [1997] found that β is approximately 1 for the ionization of H, O, O_2 and N_2 specifically. *Ribas et al.* [2005] used six stars with a range of ages from 0.1 to 6.7 Gyr and found β values of 1.20 and 1.23 for the wavelength ranges 10-36 and 0.1 - 110 nm respectively. *Tu et al.* [2015] combined a stellar rotational evolution model with observations of hundreds of stars in young stellar clusters and found β = 1.22 for 10-90 nm. Therefore, for this study, we will adopt β = 1.2 and leave to future work a more detailed analysis where β has rigorous uncertainties and wavelength dependence. Our expression for the time evolution of the ionization frequency I_{past} is thus:

$$I_{past} = I_{present}\left(\frac{t_{past}}{4.5\ Gyr}\right)^{-1.2} \quad (4)$$

where $I_{present}$ is the mean of the ionization frequency from the 70-year reconstructed record FISM-M shown in Figure 10a: 4.3 x 10^{-7} s^{-1} and t_{past} is the age of Mars at some point in the past in billions of years. The resulting estimate of ionization frequency over solar system history is shown in Figure 11a.

We assume the modern-era mean of 4.3 x 10^{25} O atoms per second (see previous section) for the present-day escape rate $R_{present}$ and scale up past escape rates R_{past} according to the power law dependence on ionization frequency from equation 3.

$$R_{past} = R_{present}\left(\frac{I_{past}}{I_{present}}\right)^{\gamma} = R_{present}\left(\frac{t_{past}}{4.5\ Gyr}\right)^{-1.2\gamma} \quad (5)$$

Recasting in terms of billions of years ago:

$$R_{past} = R_{present}\left(\frac{4.5}{4.5 - t_{Gyr\ ago}}\right)^{1.2\gamma} \quad (6)$$

We then use the best-fit and 1-sigma range of power law indices derived in Section 4.2 (and shown in Figure 7) to extrapolate O escape rates and cumulative loss back to 4.4 Gyr ago, shown in Figure 11b and c respectively. For comparison, we also show the very simplistic and unrealistic case of simply extrapolating current escape rates back to the early solar system (blue dashed lines) and a linear EUV dependence from the theoretical result of [*Cravens et al.*, 2016] (red dashed lines). Table 4 gives the same information in tabular form, for 0, 1, 2, 3, 3.5 and 4 billion years ago, where the 10th and 90th percentiles shown are from the distribution of 1-sigma values of power law indices shown in Figure 7b. Figure 12 shows the shape of these distributions explicitly, both in terms of escape rates (left column) and cumulative loss (right column).

Figure 11 and Figure 12 demonstrate clearly the importance of constraining the functional dependence of photochemical escape fluxes on ionization frequency (which is determined by solar EUV irradiance). For example, 6 times higher EUV at 3.5 Gyr ago leads to 6 times higher escape if the power law index 1 (i.e. linear dependence, per the theoretical model of *Cravens et al.* [2016]), but 53 times higher if the index is 2.2. Therefore, better constraining the EUV dependence of photochemical escape rates is a primary concern as more data is collected during MAVEN's extended mission.

There are three caveats to mention here. The first is that these extrapolations do not incorporate the variability in modern escape fluxes we have both observed in the MAVEN data set and inferred over the modern era (Section 4.4); for reference, the inferred modern escape rate range is shown with a green vertical bar in Figure 11b. The second is that we have not assumed any uncertainty in the historical EUV flux, though some undoubtedly exists and may be significant. While the stellar irradiance-versus-age curves derived by *Ribas et al.* [2005] do not seem to have large error bars, the 10^{th}, 50^{th} and 90^{th} percentiles for the time-decay exponent β in young stellar clusters derived by *Tu et al.* [2015] are 0.96, 1.22 and 2.15. The upper end of this range would certainly make for substantially higher inferred escape fluxes at early times. The third and most important caveat is that we should not expect photochemical escape flux dependence on solar EUV to be constant throughout Martian history. While higher pressures in the past should simply push the source of escape to higher altitudes, higher EUV in the past should increase thermospheric temperatures and lead to larger columns of atomic oxygen above the O_2^+-rich region, retarding escape. Indeed, *Zhao and Tian* [2015] show that, for this reason, photochemical escape of oxygen from DR of O_2^+ is actually lower for 20 times current EUV than for 10 times current EUV. Moreover, the total relative amounts of relevant species N, C, H and O in Mars'

atmosphere should evolve over time, leading to different relative amounts of O_2^+ versus other ions near the exobase and hence a different escape picture.

Place Table 4 here

Place Figures 10 and 11 here

5 Discussion

5.1 Comparison with previous models of photochemical O escape

Let us now compare these results with the models mentioned in the introduction, for which the two Viking Lander profiles and derived global models were the only input. These models assume northern spring equinox (L_s = 0°) and low and high solar activity, and typically a solar zenith angle of 60°. Therefore, to ensure the most meaningful, "apples to apples" comparison, let us compare these with escape rates derived between Ls = 340° and 350°: 3.0 ± 1.0 x 10^{25} s^{-1}. Given the weakness of the current solar cycle, our ionization frequency (4.3 – 4.5 x 10^{-7} s^{-1}) is slightly higher than what would be called 'solar moderate'. Table 5 compares our escape rates, with modeled escape rates from several authors. Our rates fall within the range of several studies, in particular *Groller et al.* [2014], *Fox and Hac* [2014], *Chaufray et al.* [2007], *Cipriani et al.* [2007] and *Lee et al.* [2015b], whose low and high solar activity estimates bracket those from the present study.

5.2 Uncertainties and comparison with MAVEN remote estimates of photochemical escape

It is useful to compare our derived photochemical escape rates with estimates that are consistent with remote MAVEN measurements of pickup oxygen ions [*Rahmati et al.*, 2016] (~7 x 10^{25} s^{-1}) and 130.4 nm

oxygen emission [*Lee et al.*, 2015a] (5-7 x 10^{25} s^{-1}), that were mentioned in the introduction. Those measurements were taken in late 2014 near perihelion (Ls = 250°) when CO_2 ionization frequencies were 5.6-6.2 x 10^{-7} s^{-1}, i.e. 15-20% higher than our Interval 1 for which our mean derived escape rate is 5.3 x 10^{25} s^{-1} (see Table 3). Given all the sources of uncertainty, both instrumental and modeling, in the method of *Rahmati et al.* [2016], *Lee et al.* [2015a], and the present study, this represents surprisingly good agreement between the methods.

However, likely more important than these sources of error, it is important to note the following caveats in our calculations of escape fluxes reported in this paper. The first is that there may still be as-yet undetermined systematic uncertainties in the quantities measured by NGIMS and LPW (though these data sets have undergone multiple revisions as of January 2017). Since the study uses several different quantities, such systematic uncertainties may cancel one another out or may compound. The second, and potentially most important, is that the O-CO_2 collision cross-section has not yet been measured in the laboratory and the value used here from *Fox and Hac* [2014], with the angular dependence from *Kharchenko et al.* [2000], could be in error by up to a factor of 2, leading to a similar systematic uncertainty in escape fluxes. However, the fact that we see relatively good agreement between this study and *Rahmati et al.* [2016] (which did not require cross-sections) implies that the O-CO_2 cross-section may not be in error by more than a few tens of percent. Lastly we note that *Lee et al.* [2015a] modeled the coronal emission using a simulated (i.e. not measured) thermosphere and ionosphere and an O-CO_2 cross-section 40% lower than the one used in this study. Therefore, we speculate that the relatively good agreement with this study may be due to these two factors partially canceling out.

5.3 Competition between O_2^+ DR and direct O_2^+ escape.

The altitude region within a few scale heights of the exobase (~170-250 km) is critical for understanding atmospheric escape from Mars in general. As shown in **Figure 3**e and **Figure 8**f, this is the region sufficiently low in altitude that substantial amounts of O_2^+ are created, but where the mean free path is sufficiently large that energized particles (neutrals or ions) can escape in substantial numbers without first thermalizing through collisions. O can be energized through the O_2^+ dissociative recombination (DR) reaction discussed in this paper, but both O^+ and O_2^+ created in this region can also be energized by an ambipolar electric field or by direct heating via plasma waves. *Ergun et al.* [2016] modeled these processes in 1-D, showing that, under extreme conditions, direct escape of O_2^+can result in a larger O loss than DR of O_2^+, in the following manner. First, high EUV fluxes can raise electron temperatures, which in turn raises the ambipolar electric field to the point where a thermal ion can be accelerated to escape velocity. Second, electromagnetic Poynting flux from the solar wind can directly heat these ions and provide them with escape velocity. Note that we need not model plasma processes in this work since we do not assume photochemical equilibrium in our calculations. However, these processes and the resulting energization and escape of O_2^+could be responsible for reducing O_2^+ densities above the exobase and hence for some of the variability we see in photochemical O escape fluxes.

6 Conclusions and future work

The study presented in this paper is the first effort to constrain, with the relevant in situ measurements, an important atmospheric loss channel for the Mars atmosphere: the escape of hot oxygen atoms from Mars via dissociative recombination of O_2^+ ions. The derived escape rates are consistent with some of the many previous modeling efforts on this topic and with estimates of escape rates derived from other

MAVEN instruments [e.g. *Rahmati et al.*, 2016]. However the observed dependence of escape solar EUV irradiance is significantly stronger than the linear dependence expected from simplified models [*Cravens et al.*, 2016]. The physical reasons for this observed dependence remain to be explained, including the relative impact of a) seasonal influences such as gravity waves from the lower atmosphere and thermospheric winds, b) plasma transport and currents in the ionosphere and c) ionizing effects of precipitation of magnetospheric plasma.

Our goal is ultimately to understand how photochemical escape varies spatially and with respect to season and solar influences. Models validated by reproducing this behavior can then be more confidently used to determine escape rates as we iteratively add atmosphere and increase solar EUV properties appropriately as we move backward in time, in order to gain a full picture of the importance of this escape process in the climatic evolution of Mars. Therefore, until we understand these influences and separate (insofar as possible) their causes into EUV-related and solar-wind-related, extrapolations to past heliospheric conditions (as in section 4.5) will be quite uncertain beyond the uncertainties in those conditions themselves.

In future, we intend to make simultaneous estimates of O escape rates, both from pickup O ions [*Larson et al.*, 2015; *Rahmati et al.*, 2015] and in situ thermospheric/ionospheric measurements (i.e. this work) in order to constrain the crucial O-CO_2 collision cross-section. Such comparisons have not been possible due to orbit geometry, but should be in late 2016.

7 Acknowledgments

The work of all co-authors was supported by the MAVEN project. All data used in this study are publicly available at both the MAVEN Science Data Center (https://lasp.colorado.edu/maven/sdc/public/) and the Planetary Data System (http://atmos.nmsu.edu/data_and_services/atmospheres_data/MAVEN/maven_main.html). We would also like to thank the efforts of two anonymous reviewers for improving the paper substantially.

8 Appendix A: CO2 photoionization rate

In this study we investigate the dependence of photochemical escape fluxes on the sun's ability to ionize molecules in the upper atmosphere of Mars. However, it is important to choose an appropriate metric for this ability. Solar F10.7 radio emission measured on earth has been used for several decades as a proxy for the EUV irradiance which causes this ionization [*Girazian and Withers*, 2015; *Hinteregger*, 1981]. For Mars, both F10.7 and directly-measured EUV irradiance (from Earth orbit) in prominent ionizing lines (such as the 30.4 nm He-II emission), scaled and rotated from Earth to Mars, have been used to study the effects of photoionization [*Lillis et al.*, 2010; *Withers*, 2009]. EUV irradiance at Mars is measured by the MAVEN Extreme Ultraviolet Monitor (EUVM) in 3 key wavelength ranges [*Eparvier et al.*, 2014]. These measurements, plus full-spectrum measurements from Earth, are used to drive an empirical model of EUV and FUV spectral irradiance at Mars, called the Flair Irradiance Special Model for Mars (FISM-M) [*Thiemann et al.*, 2016], which we take as the best estimate for this irradiance. An example of the output of FISM-M is shown in Figure 13.

However, to derive the most appropriate metric for solar radiation's ability to produce O_2^+ ions, we must convolve this irradiance spectrum with the photoionization cross-section for CO_2 (since CO_2^+ is by far the dominant source of O2+ via the reaction $CO_2^+ + O \rightarrow CO + O_2^+$). This convolution is shown in Figure 13, panels b), c) and d), whereby differential photon flux (panel b) is multiplied by photoionization cross-section (panel c), to arrive at differential ionization frequency (panel d). We integrate this differential ionization frequency with respect to wavelength to get total ionization frequency, which is the metric used throughout this manuscript.

Place Figure 12 here.

9 References

Andersson, L., R. E. Ergun, G. Delory, A. I. Eriksson, J. Westfall, H. Reed, J. F. Mccauley, D. J. Summers, and D. Meyers (2015), The Langmuir Probe and Waves Experiment for MAVEN, *Space Science Reviews*.

Andrews, D. J., L. Andersson, G. T. Delory, R. E. Ergun, A. I. Eriksson, C. M. Fowler, T. McEnulty, M. W. Morooka, T. Weber, and B. M. Jakosky (2015), Ionospheric plasma density variations observed at Mars by MAVEN/LPW, *Geophysical Research Letters*, *42*(21), 8862-8869, doi:10.1002/2015GL065241.

Ayres, T. R. (1997), Evolution of the solar ionizing flux, *Journal of Geophysical Research: Planets*, *102*(E1), 1641-1651, doi:10.1029/96JE03306.

Balakrishnan, N., V. Kharchenko, and A. Dalgarno (1998), Quantum mechanical and semiclassical studies of N+N2 collisions and their application to thermalization of fast N atoms, *J Chem Phys*, *108*, 943, doi:10.1063/1.475458.

Benna, M., P. R. Mahaffy, J. M. Grebowsky, J. L. Fox, R. V. Yelle, and B. M. Jakosky (2015), First measurements of composition and dynamics of the Martian ionosphere by MAVEN's Neutral Gas and Ion Mass Spectrometer, *Geophysical Research Letters*, *42*(21), 8958-8965, doi:10.1002/2015GL066146.

Bougher, S. W., S. Engel, R. G. Roble, and B. Foster (1999), Comparative terrestrial planet thermospheres 2. Solar cycle variation of global structure and winds at equinox, *Journal of Geophysical Research-Planets*, *104*(E7), 16591-16611, doi:Doi 10.1029/1998je001019.

Bougher, S. W., S. Engel, R. G. Roble, and B. Foster (2000), Comparative terrestrial planet thermospheres 3. Solar cycle variation of global structure and winds at solstices, *Journal of Geophysical Research-Planets*, *105*(E7), 17669-17692, doi:Doi 10.1029/1999je001232.

Brain, D. A., S. Barabash, S. W. Bougher, F. Duru, B. M. Jakosky, and R. Modolo (2015), Solar Wind Interaction and Atmospheric Escape, in *Mars book II*, edited.

Chaufray, J. Y., R. Modolo, F. Leblanc, G. Chanteur, R. E. Johnson, and J. G. Luhmann (2007), Mars solar wind interaction: Formation of the Martian corona and atmospheric loss to space, *Journal of Geophysical Research*, *112*(E9), doi:10.1029/2007je002915.

Cipriani, F., F. Leblanc, and J. J. Berthelier (2007), Martian Corona: nonthermal sources of hot heavy species, *Journal of Geophysical Research*, *112*, doi:10.1029/2007JE002915.

Cravens, T. E., et al. (2016), Hot Oxygen Escape from Mars: Simple Scaling with Solar EUV Irradiance, *Journal of Geophysical Research: Space Physics*, n/a-n/a, doi:10.1002/2016JA023461.

Deighan, J., et al. (2015), MAVEN IUVS observation of the hot oxygen corona at Mars, *Geophysical Research Letters*, *42*(21), 9009-9014, doi:10.1002/2015GL065487.

England, S. L., et al. (2016), Simultaneous observations of atmospheric tides from combined in situ and remote observations at Mars from the MAVEN spacecraft, *Journal of Geophysical Research: Planets*, *121*(4), 594-607, doi:10.1002/2016JE004997.

Eparvier, F., P. C. Chamberlin, and T. N. Woods (2014), The Solar Extreme Ultraviolet Monitor for MAVEN, *Space Sciences Reviews*.

Ergun, R. E., et al. (2016), Enhanced O2+ loss at Mars due to an ambipolar electric field from electron heating, *Journal of Geophysical Research: Space Physics*, *121*(5), 4668-4678, doi:10.1002/2016JA022349.

Ergun, R. E., M. W. Morooka, C. M. Fowler, G. Delory, D. J. Andrews, A. I. Eriksson, T. McEnulty, and B. Jakosky (2015), Dayside electron temperature and density profiles at Mars: first results from the MAVEN LPW instrument, *Geophysical Research Letters*.

Fillingim, M. O., R. J. Lillis, S. L. England, L. M. Peticolas, D. A. Brain, J. S. Halekas, C. Paty, D. Lummerzheim, and S. W. Bougher (2012), On wind-driven electrojets at magnetic cusps in the nightside ionosphere of Mars, *Earth Planets and Space*, *64*(2), 93-103, doi:DOI 10.5047/eps.2011.04.010.

Fowler, C. M., et al. (2015), The first in situ electron temperature and density measurements of the Martian nightside ionosphere, *Geophysical Research Letters*, *42*(21), 8854-8861, doi:10.1002/2015GL065267.

Fox, J. L., and A. B. Hac (2014), The escape of O from Mars: Sensitivity to the elastic cross sections, *Icarus*, *228*, 375-385, doi:DOI 10.1016/j.icarus.2013.10.014.

Fox, J. L., and A. B. Hać (2009), Photochemical escape of oxygen from Mars: A comparison of the exobase approximation to a Monte Carlo method, *Icarus*, *204*(2), 527-544, doi:10.1016/j.icarus.2009.07.005.

Girazian, Z., and P. Withers (2015), An empirical model of the extreme ultraviolet solar spectrum as a function of F10.7, *Journal of Geophysical Research: Space Physics*, *120*(8), 6779-6794, doi:10.1002/2015JA021436.

Gonzalez-Galindo, F., J. Y. Chaufray, M. A. Lopez-Valverde, G. Gilli, F. Forget, F. Leblanc, R. Modolo, S. Hess, and M. Yagi (2013), Three-dimensional Martian ionosphere model: I. The photochemical ionosphere below 180 km, *Journal of Geophysical Research-Planets*, *118*(10), 2105-2123, doi:Doi 10.1002/Jgre.20150.

Groller, H., H. Lichtenegger, H. Lammer, and V. I. Shematovich (2014), Hot oxygen and carbon escape from the martian atmosphere, *Planetary and Space Science*, *98*, 93-105.

Halekas, J. S., E. R. Taylor, G. Dalton, G. Johnson, D. W. Curtis, J. P. McFadden, D. L. Mitchell, R. P. Lin, and B. M. Jakosky (2015), The MAVEN Solar Wind Ion Analyzer, *Space Science Reviews*, *195*(1), 125-151, doi:10.1007/s11214-013-0029-z.

Hanson, W. B., S. Sanatani, and D. Zuccaro (1976), Retarding Potential Analyzer Measurements from Viking Landers, *Transactions-American Geophysical Union*, *57*(12), 966-966.

Hanson, W. B., S. Sanatani, and D. R. Zuccaro (1977), The Martian ionosphere as observed by the Viking retarding potential analyzers, *Journal of Geophysical Research*, *82*(28), 4351-4363, doi:10.1029/JS082i028p04351.

Hinteregger, H. E. (1981), Representations of solar EUV fluxes for aeronomical applications, *Advances in Space Research*, *1*(12), 39-52, doi:http://dx.doi.org/10.1016/0273-1177(81)90416-6.

Hodges, R. R. (2002), The rate of loss of water from Mars, *Geophysical Research Letters*, *29*(3), 1038, doi:10.1029/2001GL013853.

Huebner, W. F., and J. Mukherjee (2015), Photoionization and photodissociation rates in solar and blackbody radiation fields, *Planetary and Space Science*, *106*, 11-45, doi:http://dx.doi.org/10.1016/j.pss.2014.11.022.

Jakosky, B. M., R. P. Lin, J. M. Grebowsky, J. G. Luhmann, D. F. Mitchell, G. Beutelschies, and others (2014), The Mars Atmosphere and Volatile Evolution (MAVEN) Mission, *Space Sciences Reviews*, doi:10.1007/s11214-015-0139-x.

Johnstone, C. P., M. Güdel, I. Brott, and T. Lüftinger (2015), Stellar winds on the main-sequence. II. The evolution of rotation and winds, *Astronomy and Astrophysics*, *577*.

Keating, G. M., et al. (1998), The structure of the upper atmosphere of Mars: In situ accelerometer measurements from Mars global surveyor, *Science*, *279*(5357), 1672-1676, doi:DOI 10.1126/science.279.5357.1672.

Kharchenko, V., A. Dalgarno, B. Zygelman, and J. H. Yee (2000), Energy transfer in collisions of oxygen atoms in the terrestrial atmosphere, *Journal of Geophysical Research*, *105*(24), 24899-24906, doi:10.1029/2000JA000085.

Kim, J., A. F. Nagy, J. L. Fox, and T. E. Cravens (1998), Solar cycle variability of hot oxygen atoms at Mars, *Journal of Geophysical Research: Space Physics*, *103*(A12), 29339-29342, doi:10.1029/98JA02727.

Krestyanikova, M. A., and V. I. Shematovich (2005), Stochastic models of hot planetary and satellite coronas: a photochemical source of hot oxygen in the upper atmosphere of Mars, *Solar System Research*, *39*(1), 22-32, doi:10.1007/s11208-005-0002-9.

Lammer, H., J. F. Kasting, E. Chassefiere, R. E. Johnson, Y. N. Kulikov, and F. Tian (2008), Atmospheric Escape and Evolution of Terrestrial Planets and Satellites, *Space Science Reviews*, *139*(1), 399-436, doi:10.1007/978-0-387-87825-6_11.

Larson, D., et al. (2015), The MAVEN Solar Energetic Particle Investigation, *Space Science Reviews*, 1-20, doi:10.1007/s11214-015-0218-z.

Lee, Y., M. R. Combi, V. Tenishev, S. W. Bougher, J. Deighan, N. M. Schneider, W. E. McClintock, and B. M. Jakosky (2015a), A comparison of 3-D model predictions of Mars' oxygen corona with early MAVEN IUVS observations, *Geophysical Research Letters*, *42*(21), 9015-9022, doi:10.1002/2015GL065291.

Lee, Y., M. R. Combi, V. Tenishev, S. W. Bougher, and R. J. Lillis (2015b), Hot oxygen corona at Mars and the photochemical escape of oxygen: Improved description of the thermosphere, ionosphere, and exosphere, *Journal of Geophysical Research: Planets*, *120*(11), 1880-1892, doi:10.1002/2015JE004890.

Lillis, R. J., and D. A. Brain (2013), Nightside electron precipitation at Mars: Geographic variability and dependence on solar wind conditions, *Journal of Geophysical Research-Space Physics*, *118*(6), 3546-3556, doi:Doi 10.1002/Jgra.50171.

Lillis, R. J., et al. (2015), Characterizing Atmospheric Escape from Mars Today and Through Time, with MAVEN, *Space Science Reviews*, 1-66, doi:10.1007/s11214-015-0165-8.

Lillis, R. J., D. A. Brain, S. L. England, P. Withers, M. O. Fillingim, and A. Safaeinili (2010), Total electron content in the Mars ionosphere: Temporal studies and dependence on solar EUV flux, *Journal of Geophysical Research-Space Physics*, *115*, doi:Artn A11314

Doi 10.1029/2010ja015698.

Lillis, R. J., M. O. Fillingim, and D. A. Brain (2011), Three-dimensional structure of the Martian nightside ionosphere: Predicted rates of impact ionization from Mars Global Surveyor magnetometer and electron reflectometer measurements of precipitating electrons, *Journal of Geophysical Research-Space Physics*, *116*, doi:Artn A12317

Doi 10.1029/2011ja016982.

Lillis, R. J., D. L. Mitchell, R. P. Lin, and M. H. Acuna (2008), Electron reflectometry in the martian atmosphere, *Icarus*, *194*(2), 544-561, doi:DOI 10.1016/j.icarus.2007.09.030.

Mahaffy, P. R., M. Benna, M. Elrod, R. V. Yelle, S. W. Bougher, S. W. Stone, and B. M. Jakosky (2015), Structure and composition of the neutral upper atmosphere of Mars from the MAVEN NGIMS investigation, *Geophysical Research Letters*, *42*(21), 8951-8957, doi:10.1002/2015GL065329.

Mahaffy, P. R., et al. (2014), The Neutral Gas and Ion Mass Spectrometer on the Mars Atmosphere and Volatile Evolution Mission, *Space Science Reviews*, *195*(1), 49-73, doi:10.1007/s11214-014-0091-1.

McClintock, W., N. M. Schneider, G. M. Holsclaw, J. Clarke, A. Hoskins, I. Stewart, F. Montmessin, and R. Yelle (2015), The Imaging Ultraviolet Spectrograph for the MAVEN Mission, *Space Science Reviews*, *195*(1-4), 75-124, doi:10.1007/s11214-014-0098-7.

McFadden, J., O. Kortmann, and G. J. G. Dalton, R. Abiad, D. Curtis, R. Sterling, K. Hatch, P. Berg, C. Tiu, M. Marckwordt, R. Lin, and B. Jakosky (2015), The MAVEN Suprathermal and thermal Ion Composition (STATIC) Instrument *Space Science Reviews*.

Medvedev, A. S., and E. Yigit (2012), Thermal effects of internal gravity waves in the Martian upper atmosphere, *Publication: Geophysical Research Letters, Volume 39, Issue 5, CiteID L05201*, doi:10.1029/2012gl050852.

Morgan, D. D., D. A. Gurnett, D. L. Kirchner, J. L. Fox, E. Nielsen, and J. J. Plaut (2008), Variation of the Martian ionospheric electron density from Mars Express radar soundings, *Journal of Geophysical Research*, *113*(A9), doi:10.1029/2008ja013313.

Morschhauser, A., V. Lesur, and M. Grott (2014), A spherical harmonic model of the lithospheric magnetic field of Mars, *Journal of Geophysical Research: Planets*, *119*(6), 1162-1188, doi:10.1002/2013JE004555.

Nagy, A. F., M. W. Liemohn, J. L. Fox, and J. Kim (2001), Hot carbon densities in the exosphere of Mars, *Journal of Geophysical Research: Space Physics*, *106*(A10), 21565-21568, doi:10.1029/2001JA000007.

Němec, F., D. D. Morgan, D. A. Gurnett, and D. A. Brain (2011), Areas of enhanced ionization in the deep nightside ionosphere of Mars, *Journal of Geophysical Research*, *116*(E6), doi:10.1029/2011je003804.

Nier, A. O., W. B. Hanson, A. Seiff, M. B. Mcelroy, N. W. Spencer, R. J. Duckett, T. C. D. Knight, and W. S. Cook (1976), Composition and Structure of Martian Atmosphere - Preliminary-Results from Viking-1, *Science*, *193*(4255), 786-788, doi:DOI 10.1126/science.193.4255.786.

Petrignani, A., F. Hellberg, R. D. Thomas, M. Larsson, P. C. Cosby, and W. J. van der Zande (2005), Electron energy-dependent product state distributions in the dissociative recombination of O2+, *J Chem Phys*, *122*(23), 234311, doi:10.1063/1.1937388.

Rahmati, A., et al. (2016), MAVEN measured oxygen and hydrogen pickup ions: probing the Martian atmosphere and neutral escape, *Journal of Geophysical Research*, doi: *10.1002/2016JA023371*.

Rahmati, A., D. E. Larson, T. E. Cravens, R. J. Lillis, P. A. Dunn, J. S. Halekas, J. E. Connerney, F. G. Eparvier, E. M. B. Thiemann, and B. M. Jakosky (2015), MAVEN insights into oxygen pickup ions at Mars, *Geophysical Research Letters*, n/a-n/a, doi:10.1002/2015GL065262.

Ribas, I., E. F. Guinan, M. Güdel, and M. Audard (2005), Evolution of the Solar Activity over Time and Effects on Planetary Atmospheres. I. High-Energy Irradiances (1-1700 Å), *The Astrophysical Journal*, *622*(1), 680.

Riousset, J. A., C. S. Paty, R. J. Lillis, M. O. Fillingim, S. L. England, P. G. Withers, and J. P. M. Hale (2013), Three-dimensional multifluid modeling of atmospheric electrodynamics in Mars' dynamo region, *Journal of Geophysical Research-Space Physics*, *118*(6), 3647-3659, doi:Doi 10.1002/Jgra.50328.

Schunk, R. W., and A. Nagy (2000), *Ionospheres: Physics, Plasma Physics, and Chemistry*, Cambridge Univ. Press,, New York.

Thiemann, E., P. Chamberlin, F. Eparvier, T. Woods, S. Bougher, and B. Jakosky (2016), The MAVEN/EUVM Level 3 Spectral Irradiance Model: Algorithms and Results, *Journal of Geophysical Research*.

Tu, L., C. P. Johnstone, M. Güdel, and H. Lammer (2015), The extreme ultraviolet and X-ray Sun in Time: High-energy evolutionary tracks of a solar-like star, *A&A*, *577*.

Valeille, A., M. R. Combi, S. W. Bougher, V. Tenishev, and A. F. Nagy (2009a), Three-dimensional study of Mars upper thermosphere/ionosphere and hot oxygen corona: 2. Solar cycle, seasonal variations, and evolution over history, *Journal of Geophysical Research-Planets*, *114*, doi:Artn E11006

Doi 10.1029/2009je003389.

Valeille, A., V. Tenishev, S. W. Bougher, M. R. Combi, and A. F. Nagy (2009b), Three-dimensional study of Mars upper thermosphere/ionosphere and hot oxygen corona: 1. General description and results at equinox for solar low conditions, *Journal of Geophysical Research*, *114*(E11), doi:10.1029/2009je003388.

Withers, P. (2009), A review of observed variability in the dayside ionosphere of Mars, *Advances in Space Research*, *44*(3), 277-307, doi:10.1016/j.asr.2009.04.027.

Wright, C. J. (2012), A one-year seasonal analysis of martian gravity waves using MCS data, *Icarus*, *219*(1), 274-282, doi:http://dx.doi.org/10.1016/j.icarus.2012.03.004.

Zhao, J., and F. Tian (2015), Photochemical escape of oxygen from early Mars, *Icarus*, *250*, 477-481, doi:http://dx.doi.org/10.1016/j.icarus.2014.12.032.

10 Figures

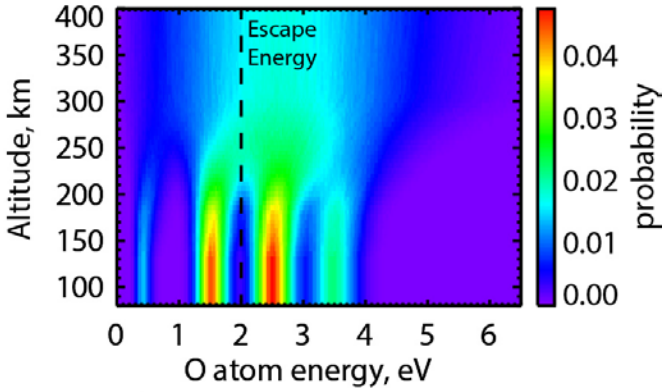

Figure 1: example probability distribution of hot O atom energies as a function of altitude. The escape energy (at 200 km) of 1.98 eV is shown with a dashed black vertical line.

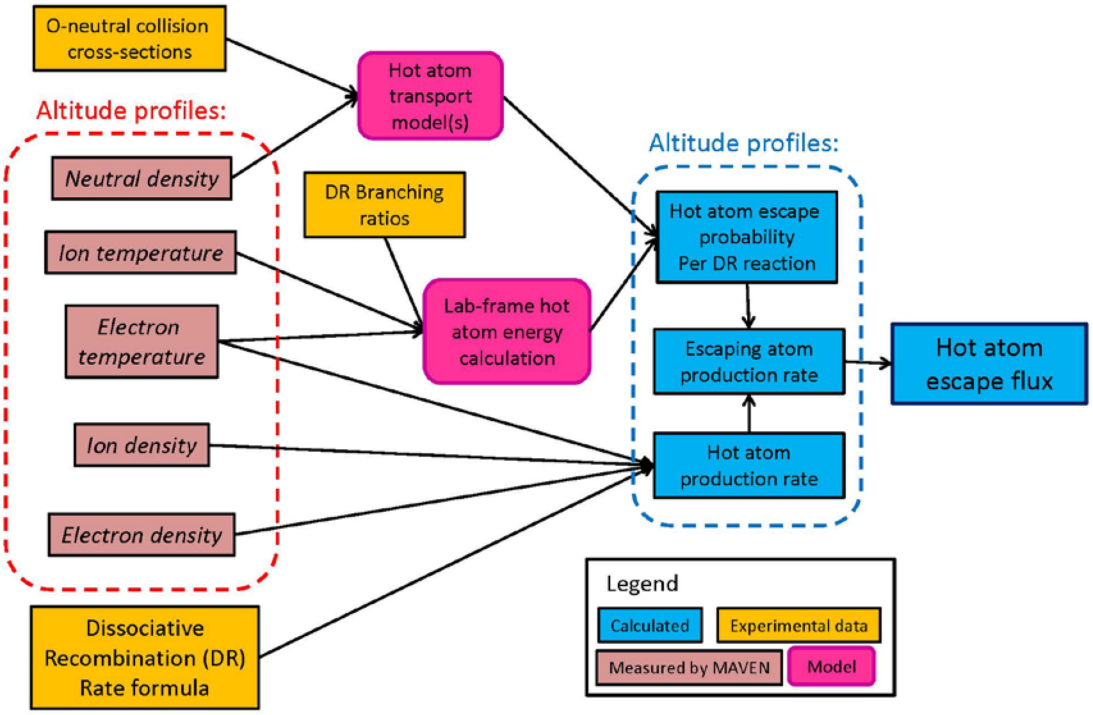

Figure 2: Flowchart explaining calculation of hot oxygen escape from measured altitude profiles of neutral densities and ion and electron densities and temperatures.

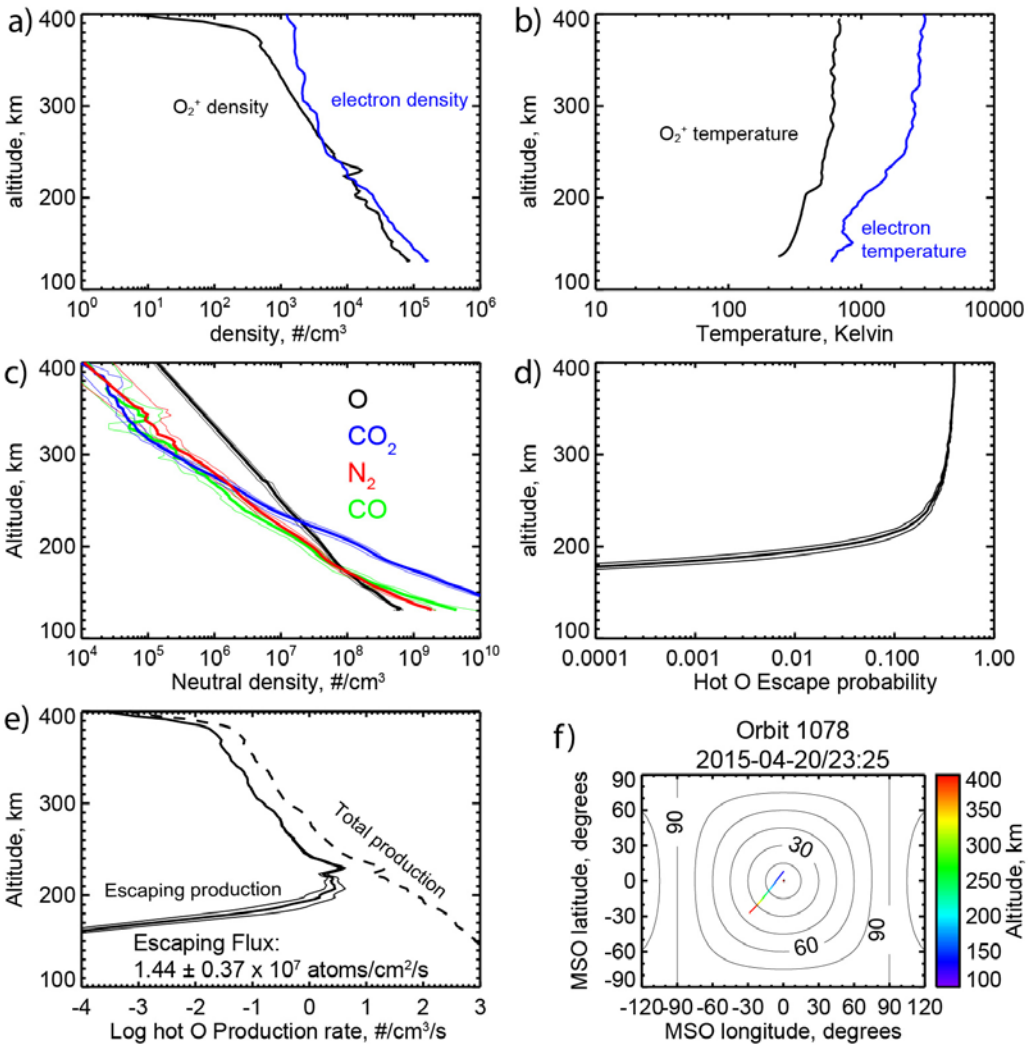

Figure 3: Example of escaping flux calculation for orbit 1078, on April 20, 2015. Panels a)-e) show altitude profiles of measured and calculated quantities (see Figure 2 for how they relate). Panel a) shows electron density (from LPW) and O_2^+ density (from NGIMS). Panel b) shows electron temperature (from LPW) and O_2^+ temperature (from STATIC). Panel c) shows neutral density profiles measured by NGIMS on the previous and subsequent orbits (thin lines) and the averages of those (thick lines). Panel d) shows the escape probabilities for hot O atoms calculated using the neutral densities from the previous and subsequent orbits (thin lines) and their averages (thick line). Panel e) shows the

production rate of hot O atoms from the dissociative recombination of O_2^+, where the dashed line shows total production and the solid lines show just the production rate of escaping atoms (thick line and thin lines correspond to those in panel d). Integrating these lines with respect to altitude gives the total escaping flux and its uncertainty, shown within panel e). Panel f) shows MAVEN's trajectory during this time in MSO coordinates, where the 15° increments in solar zenith angle are shown with contours.

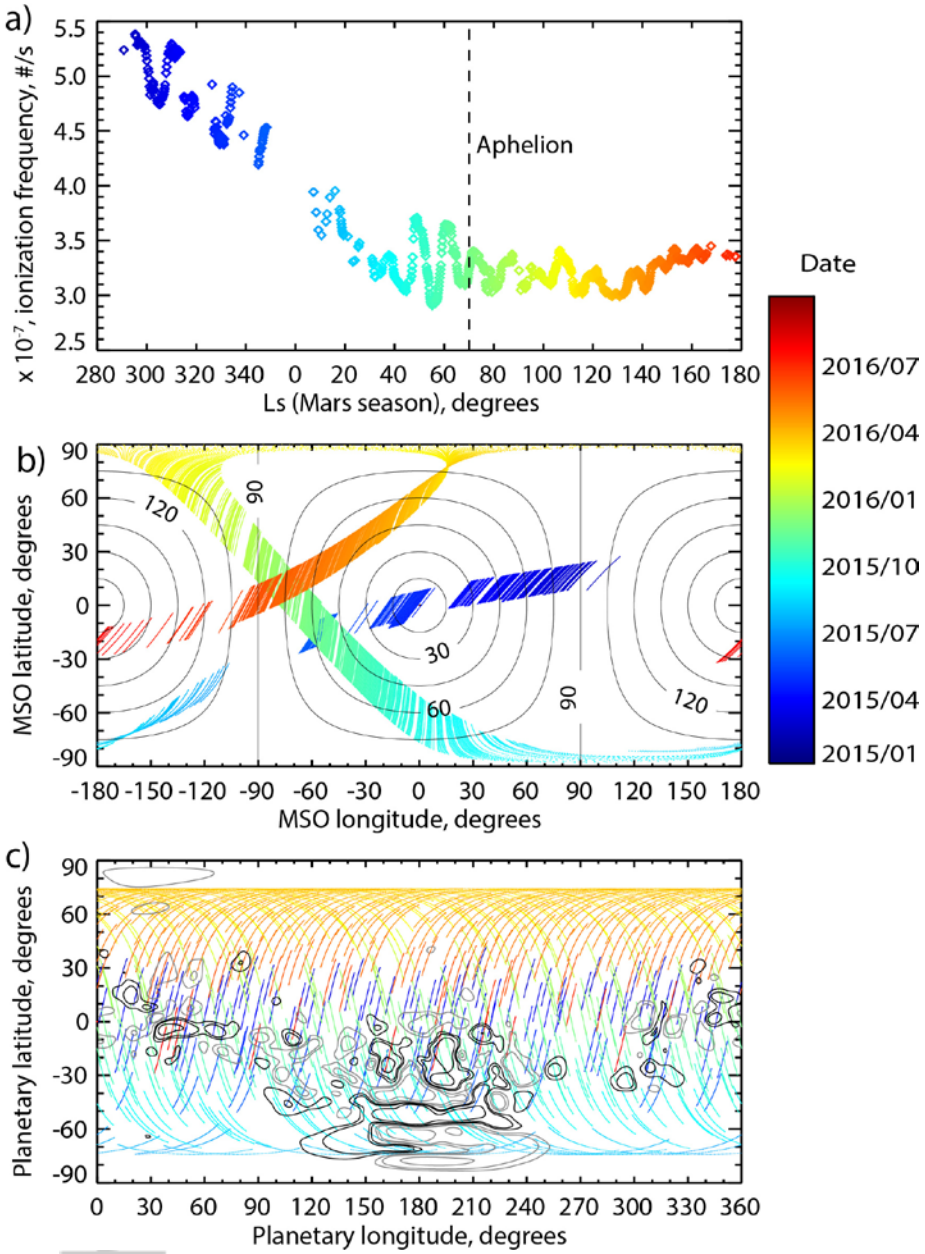

Figure 4: Data coverage for this study. All three panels are colored by date, covering 2015-02-10 to 2016-07-31. Panel a) plots CO2 photoionization frequency (see appendix A) versus Mars season (Mars year 32 and 33). Panels b) and c) plot the locations of all data taken below 250 km altitude, in MSO coordinates (15° increments of solar zenith angle are shown with contour lines) and planetary

coordinates respectively. Panel c) shows positive (black) and negative (gray) contours of crustal magnetic field at 400 km altitude at ±10, 20, 50 and 100 nT.

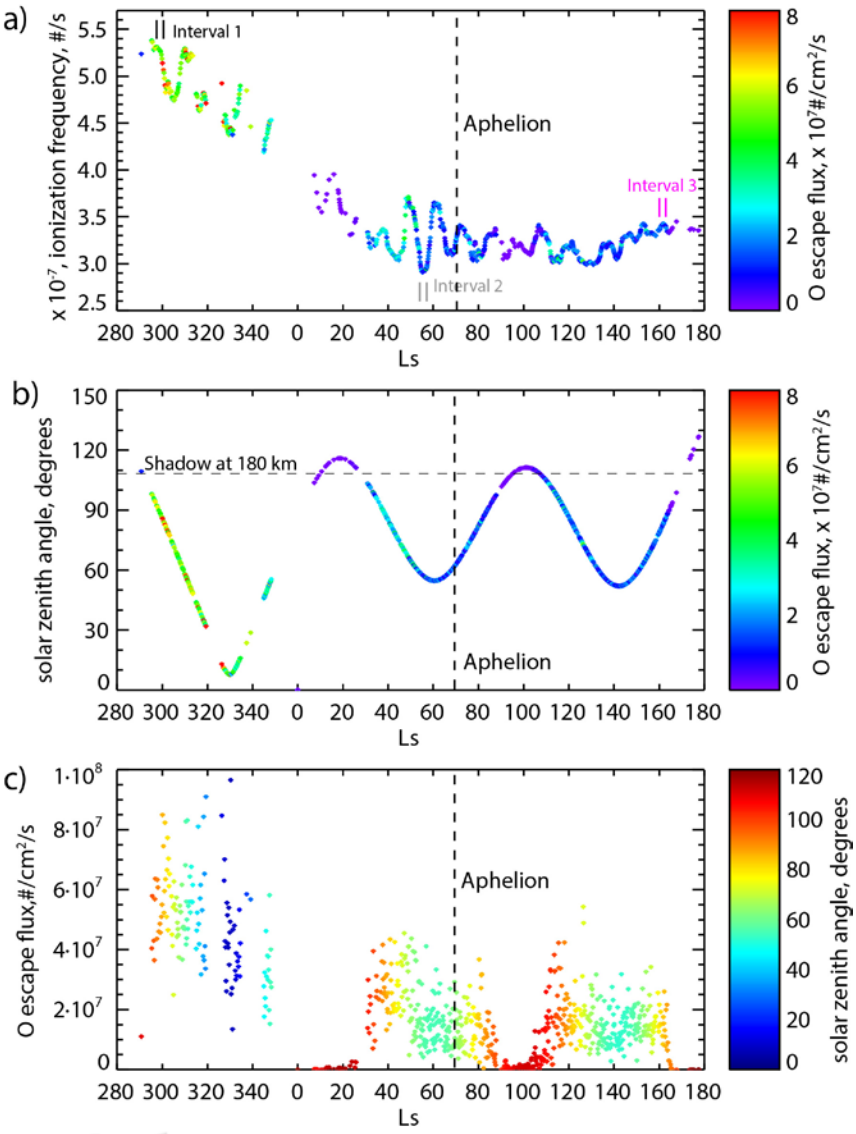

Figure 5: Derived O escape fluxes from DR of O_2^+. Panels a) and b) show escape fluxes by color as a function of Mars season (x-axis) with EUV ionization frequency (see Appendix A)and solar zenith angle on the y-axis respectively. Panel c) shows O escape fluxes as a function of Mars season (x-axis) and solar

zenith angle (colors). The vertical bars in panel a) refer to the three intervals listed in **Table 3** and discussed in Section 4.3.

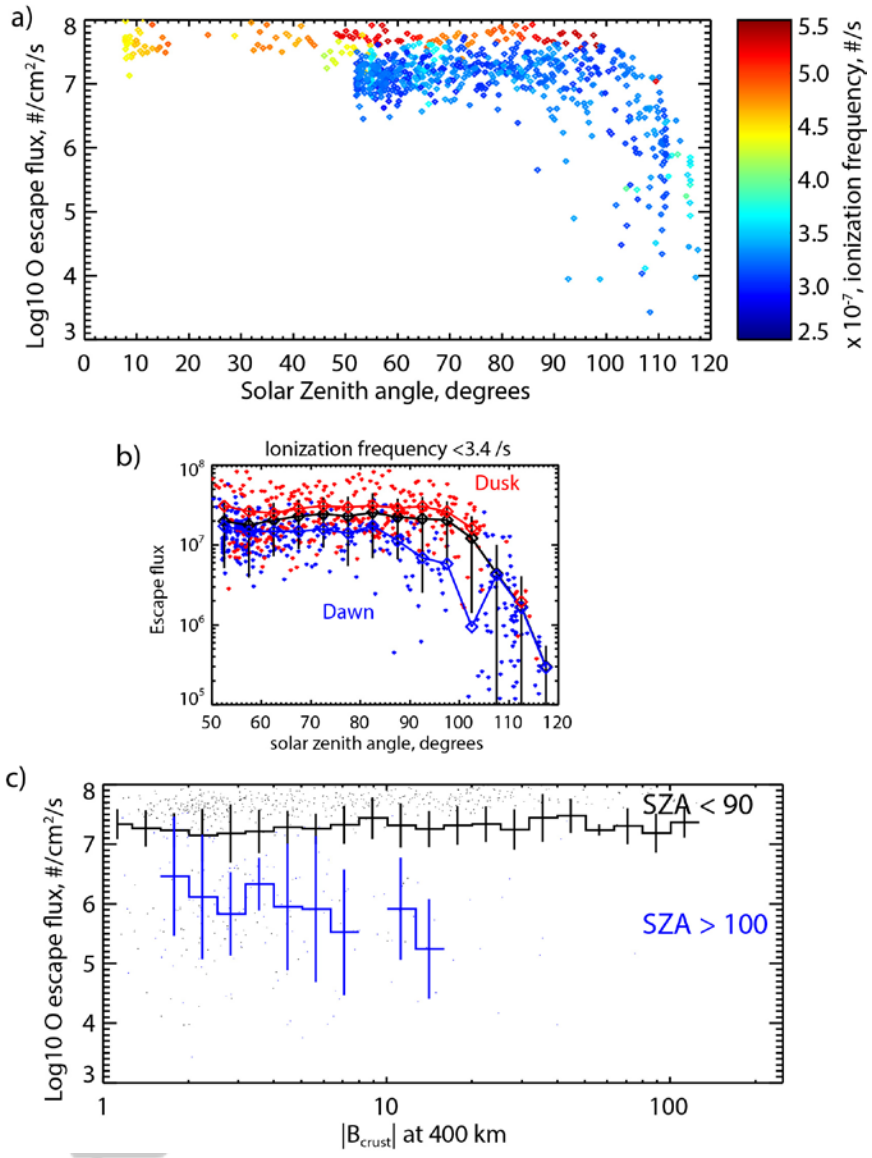

Figure 6: Derived O escape fluxes from DR of O_2^+. Panel a) shows O escape fluxes as a function of solar zenith angle at periapsis (x-axis) and photoionization frequency (see Appendix A) (colors). Panel b) shows how escape fluxes vary with solar zenith angle for low ionization frequency values (<3.4 s^{-1}) separately for dawn (blue) and dusk (red) sides of the planet. Small diamonds are individual escape flux

measurements while large black diamonds are binned averages. Panel c) shows O escape fluxes and their standard deviations binned by the crustal magnetic field strength from the low-noise crustal magnetic field model of *Morschhauser et al.* [2014] evaluated at 400 km altitude above the periapsis location, with dayside periapses shown in black and nightside in blue.

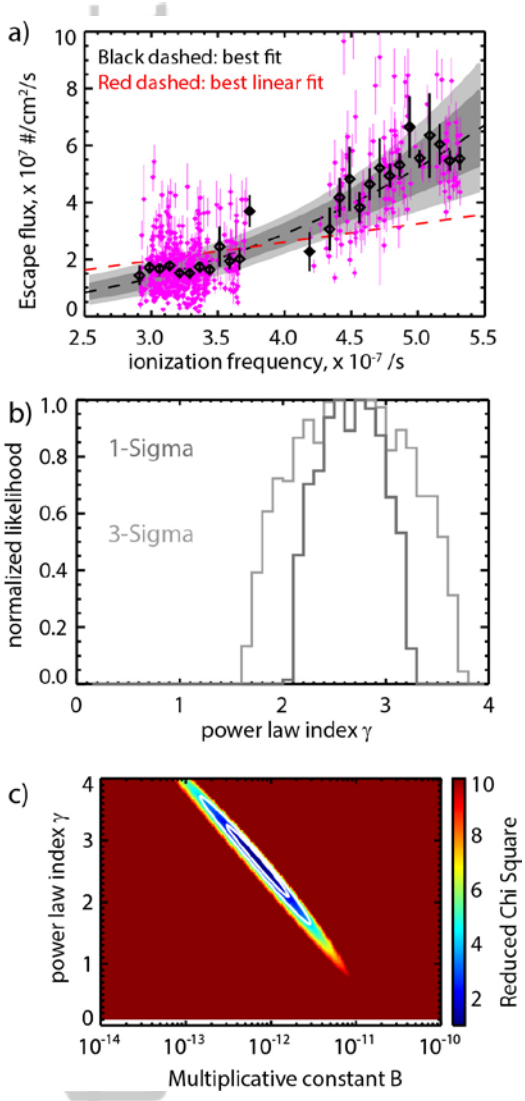

Figure 7: Dependence of dayside O escape fluxes on CO_2 photoionization frequency. Panel a) shows all 594 individual dayside (SZA <95°) derived escape flux values (small pink dots with error bars) and binned values (black diamonds) with standard errors (standard deviations divided by the square of the number of samples) in each bin. All power law fits to these binned averages that fall within the 1-

sigma and 3-sigma error ellipsoid are shown as dark and light gray lines respectively. The best fit (power law index of 2.64) is shown in black. A dashed red line shows the best linear fit that goes through the origin. Panel b) shows a histogram of the power law indices for each fit that lies within the 1-sigma (dark gray) and 3-sigma (light gray) error ellipsoids. Panel c) shows the chi-square surface for these fits as a function of the power law index and the constant term, with white contour is drawn for 1 and 3-sigma error ellipsoids. The reduced chi-squared minimum is ~1.1, which is consistent with a model appropriately fitting the data and uncertainties being estimated appropriately

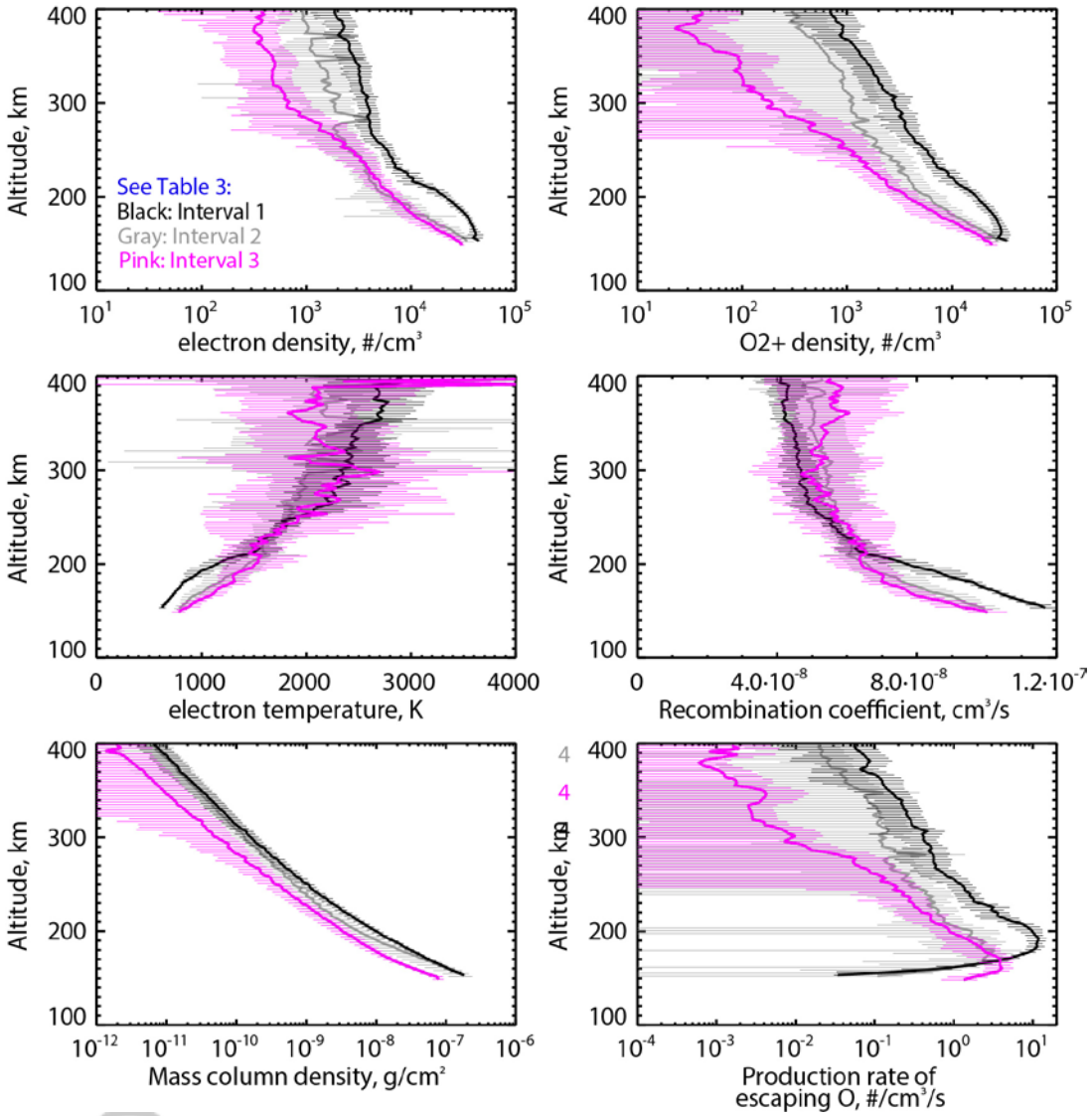

Figure 8: Examination of three particular intervals in the data set (details in table 3 and Figure 5). Intervals 1, 2 and 3 are denoted by black, gray and pink respectively. All panels show means and standard deviations, as a function of altitude: a) electron density, b) O_2^+ ion density, c) electron temperature, d) dissociative recombination rate coefficient (which depends only on electron temperature), e) mass column density above each altitude and f) production rate of escaping hot O atoms.

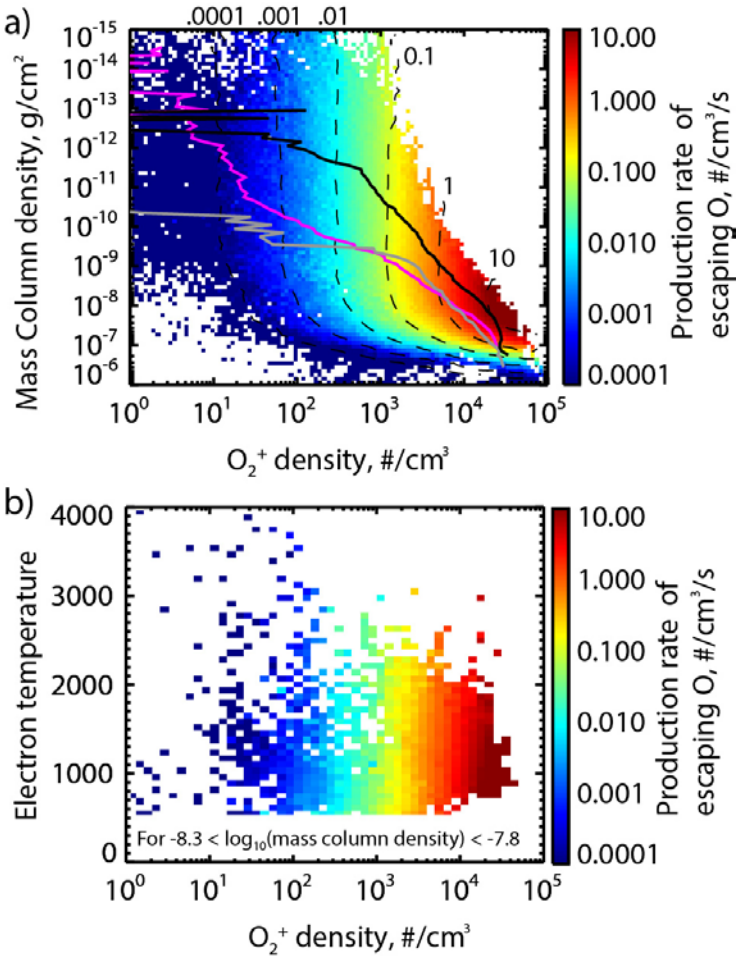

Figure 9: a) shows binned averages of the production rate of escaping hot O atoms as a function of column mass density (on an inverted scale so that its logarithm is a proxy for altitude) and O_2^+ density. Superimposed are the paths taken through this two-dimensional parameter space for the averages of each of the three intervals, using the same colors used in Figure 8 and **Table 3**. Note that the total escape flux is the integral (with respect to altitude) along such paths. Panel b) shows binned averages of the production rate of escaping hot O atoms as a function of electron temperature and O_2^+ density for a narrow range of column mass density (0.5 to 1.6 x 10^{-8} g/cm^2), showing the relatively moderate effect of electron temperature.

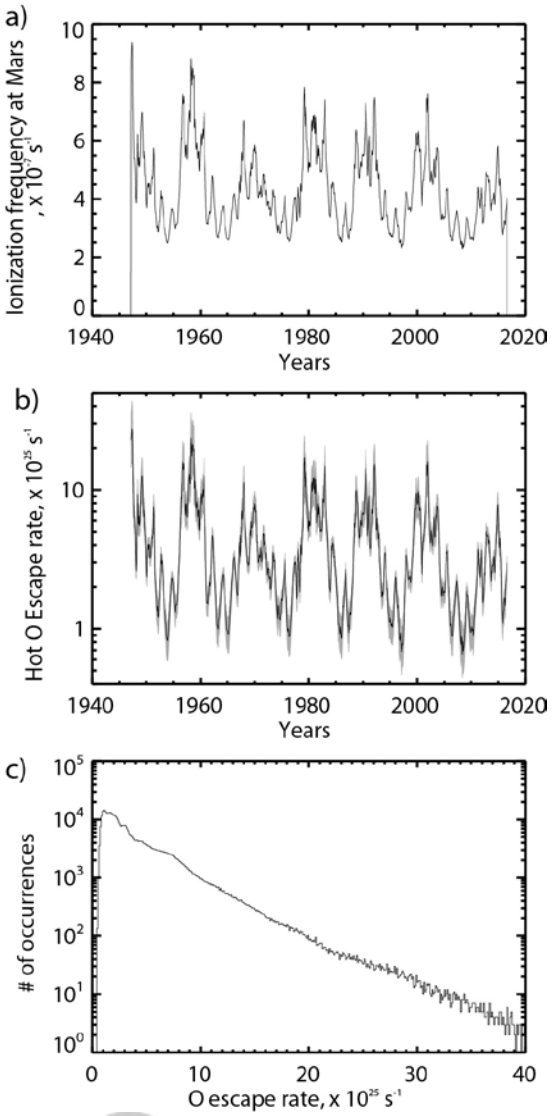

Figure 10: Estimate of photochemical escape fluxes in the modern era. Panel a) shows the weekly irradiance at 30.4 nm calculated at Mars by FISM-M since 1947 [*Thiemann et al.*, 2016]. Panel b) shows the range of escape rates over the same time that are consistent with the power law indices within the 1-sigma χ^2 error ellipsoid of fits to the EUV dependence of derived escape rates shown in Figure 7. Panel c) shows a histogram of every escape rate data point in panel b).

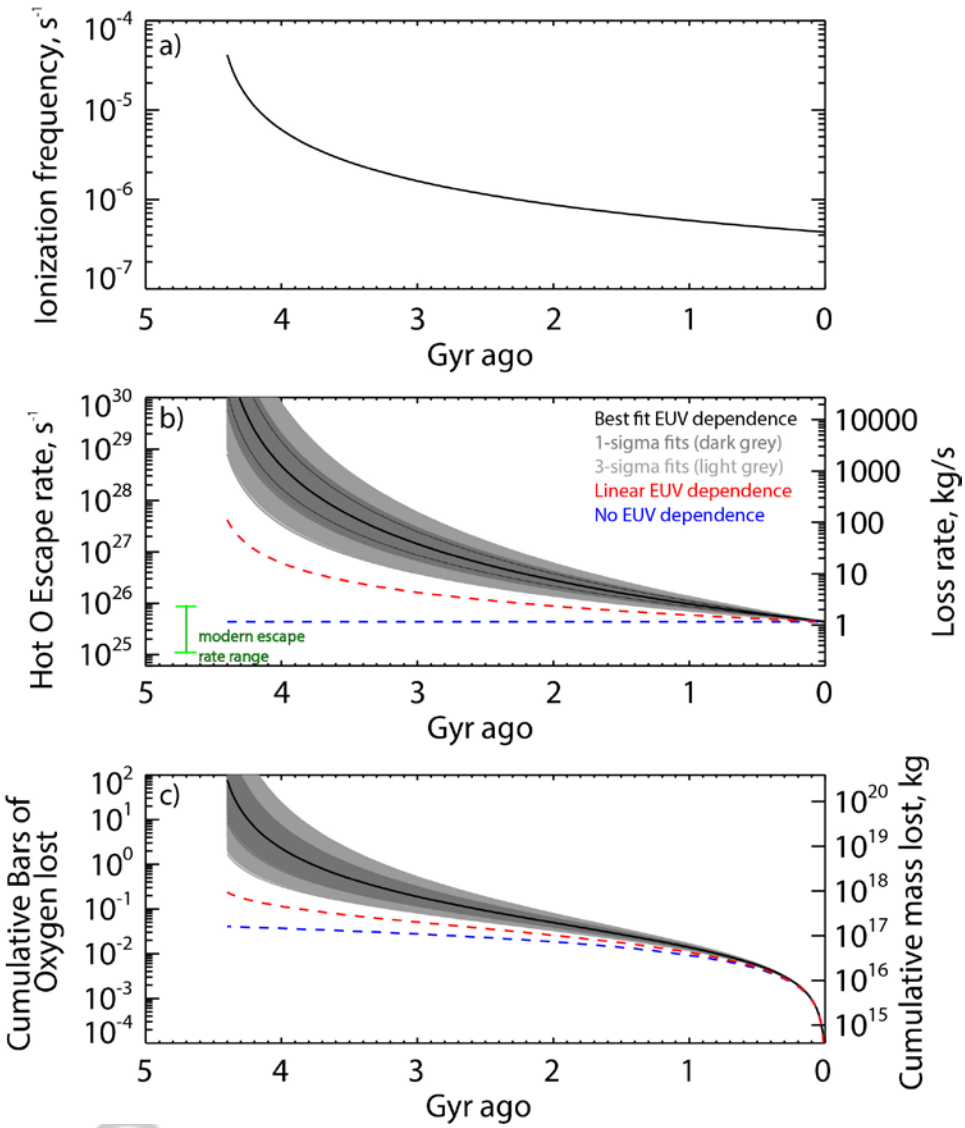

Figure 11: Extrapolation of photochemical O escape rates over Martian history. Panel a) shows the assumed history of 30.4 nm EUV irradiance, taken from *Ribas et al.* [2005]. Panels b) and c) shows the resulting escape rates and cumulative oxygen lost respectively, assuming the best power law fit (1.78) to EUV dependence (thick black), the range of 1-sigma power law fits shown in Figure 7 (gray), the 10th and 90th percentiles of those distributions (thin black), a linear dependence (red dashed) [*Cravens et al.*, 2016] and no EUV dependence, i.e. a simple extrapolation back in time of the present-day escape rate (blue dashed). The green vertical bar in panel b) shows the 1-sigma range of escape rates over the modern era.

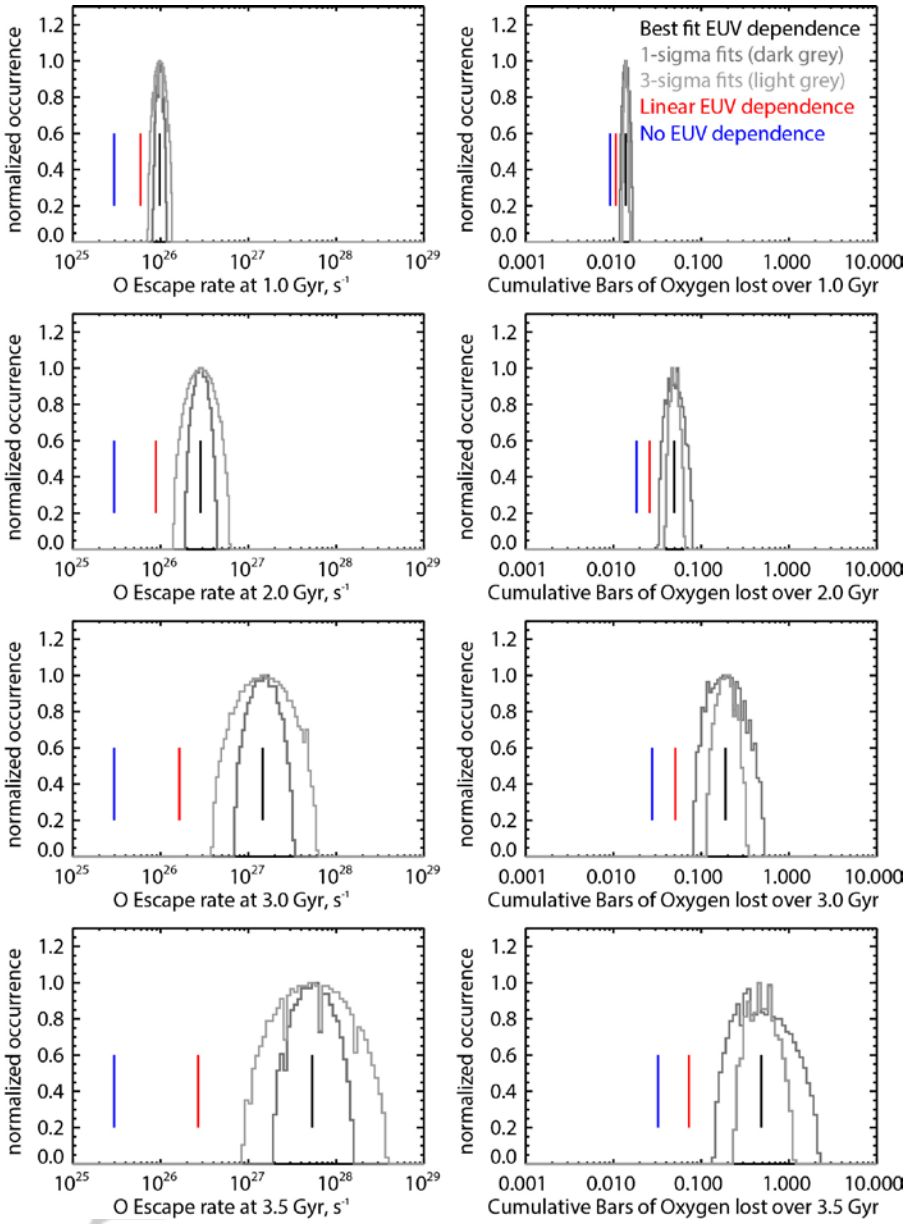

Figure 12: Probability distributions for escape rates (left column) and cumulative loss of oxygen (right column) over Martian history, with the first through fourth rows reflecting 1, 2, 3 and 3.5 billion years ago respectively. Vertical black, red and blue lines reflect values of escape rates and cumulative losses for different assumptions of EUV dependence: best fit from Figure 7 (black), linear (red) [*Cravens et al.*, 2016], and none (blue).

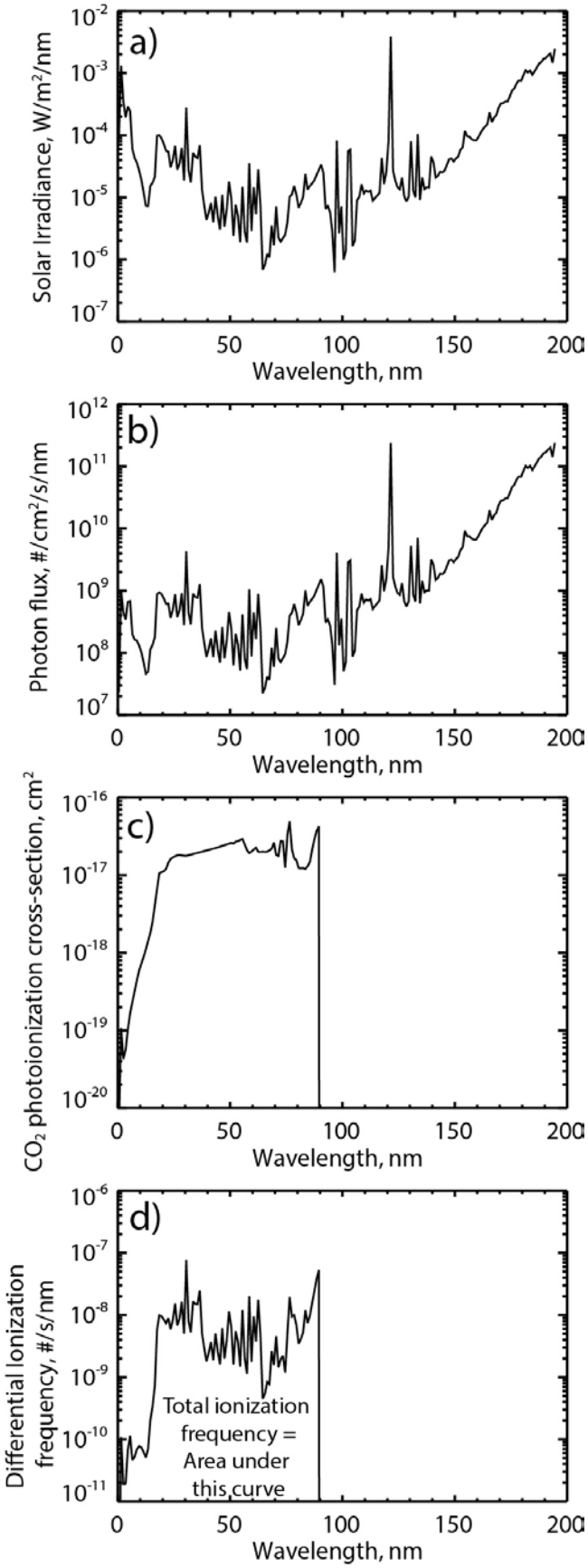

Figure 13: calculation of total ionization frequency. All panels are shown as a function of wavelength. Panel a) shows a typical solar irradiance spectrum output from FISM-M. Panel b) shows this irradiance converted to differential photon flux. Panel c) shows CO2 photoionization cross-sections from *Huebner and Mukherjee* [2015]. When multiplied together, panels b) and c) result in panel d), which is the differential ionization frequency, which is integrated over wavelength to provide total ionization frequency, as shown in several figures in this paper.

11 Tables

Table 1: The four non-negligible branches of the O_2^+ dissociative recombination reaction and their likelihoods (i.e. branching ratios).

Initial state	Final state	Likelihood
$O_2^+ + e \rightarrow$	$O(^3P) + O(^3P) + 6.99$ eV	26.5%
	$O(^1D) + O(^3P) + 5.02$ eV	47.3%
	$O(^1D) + O(^1D) + 3.06$ eV	20.4%
	$O(^1D) + O(^1S) + 0.83$ eV	5.8%

Table 2: Cross-sections for oxygen collisions with neutral species used in the hot O transport calculations.

Collision Process	**Cross-section**	**Reference**
O strikes CO_2	2.0×10^{-14} cm^2	[*Fox and Hac*, 2014]
O strikes O	0.6×10^{-14} cm^2	[*Kharchenko et al.*, 2000]
O strikes N_2	1.8×10^{-14} cm^2	[*Balakrishnan et al.*, 1998]
O strikes CO	1.8×10^{-14} cm^2	Assume same as N_2 above

Table 3: the dates, prevailing conditions and derived O escape fluxes (and standard deviations) for each of the three intervals.

Interval	1 (**Black**)	2 (Gray)	3 (Pink)
Dates	2015-02-25 to 2015-03-01	2015-10-13 to 2015-10-19	2016-05-29 to 2016-06-03
Ls	297°-301°	54°-57°	160°-163°

IAU Latitude	31°-34° North	34°-39° South	38°-42° North
MSO Latitude	22°-24° North	48°-55° South	13°-17° North
SZA	85° to 92°	56° to 59°	78° to 86°
Local time	16.7-17.1	11.2 - 11.8	6.0-6.5
Ioniz. freq., 10^{-7} #/s	5.26 ± 0.06	2.94 ± 0.04	3.40 ± 0.02
O escape flux (x10^{7} /cm^{2}/s)	5.4 ± 1.3	1.2 ±0.8	1.4±0.5

Table 4: Extrapolation of photochemical O escape rates from dissociative recombination of O_2^+ and resulting cumulative loss of oxygen over Martian history.

	Present	1 Gyr	2 Gyr	3 Gyr	3.5 Gyr	4 Gyr
Ionization frequency (x 10^{-7} s^{-1})	4.3	5.8	8.8	16	26	62
O Escape rates x 10^{25} s^{-1}						
Best fit EUV dependence	4.3	9.7	28	146	534	4990
(10^{th}, 90^{th} percentiles of extrapolated escape rates)	-	(8.7, 11.1)	(22, 38)	(88, 253)	(270, 1140)	(1800, 15000)
Linear EUV dependence	4.3	5.9	8.8	16	27	62
No EUV dependence	4.3	4.3	4.3	4.3	4.3	4.3
Total oxygen lost (mbars)						
Best fit EUV dependence	0	13.9	49.3	189	483	2250
(10^{th}, 90^{th} percentiles)	0	(13.0, 14.8)	(42, 59)	(136, 278)	(270, 850)	(1000, 5500)
Linear EUV dependence	0	10.7	25.8	51	73	114
No EUV dependence	0	9.2	18.4	27.6	32	37

Table 5: Solar cycle variability in modeled photochemical escape rates of atomic oxygen from Mars, compared with calculated escape rates from this study. Rates are given in units of 10^{25} s^{-1}.

This study	L_S = 345°-348°, moderate solar activity, 46-55° SZA	
(lower bound, mean, upper bound)	1.0, 2.0, 3.0	
Reference	L_S = 0°, Low solar activity	L_S = 0°, High solar activity
Groller et al. [2014]	1.5	2.1
Fox and Hac [2014]eroded	0.94	1.9
Fox and Hac [2014]non-eroded	1.8	4.3
Valeille et al. [2010]	3.8	13.0

Chaufray et al. [2007]	1.0	4.0
Cipriani et al. [2007] case A	0.55	2.6
Cipriani et al. [2007] case B	3.4	8.5
Krestyanikova and Shematovitch [2006]	4.5	
Hodges [2002]	4.4	18.0
Kim et al. [1998], corrected by *Nagy et al.* [2001]	3.4	8.5
Lee et al. [2015b]	1.4	3.1